Universidad Pública de Navarra

Master Thesis

Thermal-optoacoustic model for cardiac radiofrequency ablation

Author:

Francisco Javier Oyaga Landa

IBMI Supervisor:

Prof. Dr. Razansky, Daniel

Dr. Deán Ben, Xosé Luis

Dr. Pang, Genny

UPNA Supervisor:

Trigueros Malanda, Armando

Faulín Fajardo, Javier

Sánchez Corpas, Alberto

A thesis submitted in fulfillment of the requirements for the degree of Industrial Engineering

Helmholtz Zentrum münchen

Institute of Biological and Medical Imaging

Tuesday 24th March, 2015

Institute of Biological and Medical Imaging

HelmholtzZentrum münchen
Deutsches Forschungszentrum für Gesundheit und Umwelt

upna Universidad Pública de Navarra Nafarroako Unibertsitate Publikoa

"The significant problems we have cannot be solved at the same level of thinking with which we created them."

— Albert Einstein

Acknowledgements

I would like to express my appreciation and thanks to my advisor Dr. Xosé Luis Deán, you helped me when I most needed and taught me what it takes to be one of the best ones. I would like to thank to my advisor Genny Pang, for giving me the opportunity of joining this research. I would also like to thank Prof. Dr. Daniel Razansky for being a great leader and supporting my research. I would also like to thank, Armando Malanda, Javier Faulín and Alberto Sánchez for being ready whenever I contacted them, making comments to improve my research and being present today in my defense.

A special thanks to the best advisors one can count with, my parents. Words cannot express how grateful I am to my mother, and father for all of the sacrifices that you have made on my behalf. A special thanks to my family. I would also like to thank all of my friends who supported me, and incented me to strive towards my goals.

Contents

List of Figures

Abbreviations

RF	**R**adio-**F**requency
OA	**O**pto**A**coustic
US	**U**ltra**S**ound
FDM	**F**inite **D**ifference **M**ethod
FEM	**F**inite **E**lement **M**ethod
OD	**O**ptical **D**ensity
FTCS	**F**orward in time **C**entered in **S**pace
BTCS	**B**ackward in time **C**entered in **S**pace

Physical Parameters

Grüneisen Coefficient	Γ	dimensionless
Volume thermal expansivity	β	$\%K^{-1}$
Sound Speed	C_s	$m{\cdot}s^{-1}$
Specific heat capacity at a constant pressure	C_p	$kJ/kg°\mathrm{C}$
Absorption Coefficient	μ_a	cm^{-1}
Scattering Coefficient	μ_s	cm^{-1}
Effective attenuation coefficient	μ_{eff}	cm^{-1}
Optical Fluence	ϕ	J/cm^2
Anisotropy Factor	$\mathbf{g}$	—
Heat Capacity at constant pressure	C_p	$J/(kg{\cdot}K)$
Thermal Diffudivity	α	m^2/s

Chapter 1

Introduction

1.1 Optoacoustic Imaging of Radiofrequency Ablation

Radio-frequency (RF) ablation is a treatment that deliberately destroys (ablates) unwanted tissue by heating the target area with high frequency alternating current (350-500 kHz). During RF ablation a catheter electrode is inserted into the target tissue region under imaging guidance. Another electrode is placed outside the body so that a tissue volume surrounding the catheter is destroyed by heating via RF electric current. One of the main applications of this procedure is RF ablation of the heart, where the objective is to destroy abnormal pathways that are contributing to cardiac arrhythmias. RF is preferred over previously used low frequency AC or pulses of DC because it does not directly stimulate nerves or heart muscle and therefore can often be used without the need for general anesthetic. Also, RF ablation is very specific for treating the diseased tissue without significant collateral damage in adjacent areas.[Kim et al., 1994]

Optoacoustic (OA) imaging is a promising tool to provide real-time feedback on lesion formation during cardiac RF ablation. This hybrid modality combines the high-contrast and specificity of optical imaging with the high spatial resolution of ultrasound (US) imaging. OA images can be regarded as an US images in which

the contrast is provided by the optical properties of the tissue, specifically optical absorption, instead of mechanical or elastic properties.[Wang and Wu, 2007]

OA images are generated by exciting the tissue with time-varying laser light (typically short pulses). Part of the energy is absorbed by the chromophores and converted into heat by vibrational and collisional relaxation, which in turn produces an initial pressure increase that propagates to the surface and is eventually detected with an ultrasound transducer. Assuming that stress-confinement conditions are verified (it is the case when using nanosecond optical pulses), the contrast or initial pressure of the OA image can be taken to be proportional to the absorbed optical energy distribution ($H(r) = \mu_a(r) F(z)$ where; $\mu_a(r)$ = absorption coefficient and $F(z)$ = fluence distribution) and the Grüneisen coefficient ($\Gamma = \beta c^2/C_p$, where β is the volume thermal expansivity, c the sound speed and C_p the specific heat capacity at constant pressure). The Grüneisen coefficient changes with the temperature of the tissue, and hence the initial pressure $p_0(r) = \Gamma \mu_a(r) F(z)$ is also dependent on temperature in the range of interest 10-60 °C.[Beard, 2011]

Optical imaging can provide greater tissue differentiation and specificity than US as differences in optical absorption between different tissue types can be much larger than those in acoustic impedance. The OA signal is expected to change in areas where tissue has been damaged, coagulated tissue, or heated but still undamaged. Indeed, the OA signal speed significantly changes with the temperature of the tissue. When the temperature of the tissue during RF ablation is higher than 50 °C, irreversible changes that affect electrical tissue's properties take place. The irreversible changes, as coagulation, are mainly due to changes at the cellular level of cell membrane properties and dehydration resulting in a permanent increase in electrical conductivity.

OA signals ($p_0(r)$) from the treated tissue area provide feedback on the tissue properties related to the tissue coagulation level (which results in changes in optical absorption) and temperature. Decoupling these parameters, optical absorption and temperature, requires developing an accurate thermal heating model of the ablation process. By coupling the latter thermal model to a temperature-dependent

OA model we expect to be able to predict the temperature of the tissue from the OA signal given by an OA imaging system. Accurate measurement of the temperature may also help improving the reconstructed images by accounting for heterogeneities in the speed of sound. Moreover, knowing the temperature of the tissue is important in an ablation process to predict unwanted damage. Even if damage can be noticed with image guidance, feedback is only provided once damage is done. The purpose of this project is to be able to predict and keep track of temperature of the tissue to avoid damage in undesired areas. Furthermore, the temperature model and optoacoustic model is expected to help calibrating optoacoustic measurements.

1.2 Objectives, Motivation and Approach

The global objective of this thesis is to develop and validate a thermal model to predict the temperature of the tissue from an OA signal during thermal heating by radiofrequency ablation. In this way, we expect to demonstrate capabilities of OA imaging in temperature monitoring during RF ablation so that temperature maps of the tissue can be obtained during future ablation experiments.

To get to the long term goal of developing a thermal-optoacoustic model, we will first aim to develop and validate a thermal model based on transient heat transfer theory. We aim to compare different analytical and numerical approaches to model the temperature in order to be able to choose the most accurate method. We further intend to validate the developed model in phantoms experiments and check whether it can be accurate for higher temperatures.

Chapter 2

Background

This chapter provides a description of the basic principles of radio-frequency ablation and optoacoustic imaging in order to contextualize the methodology developed in this work.

2.1 Radio-frequency Ablation

Radio-frequency ablation (RFA) of the heart is a mediccal procedure that is performed in order to correct disturbances in the heart rhythm. Herein we describe the normal behavior of the heart rhythm along with problems that we can find in heart muscle and how to treat them with RFA.

2.1.1 Cardiac Arrhythmia

Heart muscle cells are stimulated by electrical impulses that cause them to contract in a uniform way and with a regular rate. These contractions produce the heartbeat, which causes blood to be pumped out of the heart into arteries and then to the rest of the body.

In a normal heart, electrical impulses arise from an area of specialized cells called the sinus node, which represents the normal pacemaker of the heart. The sinus

node is located in the right atrium, the upper right chamber of the heart. In some cases, the electrical impulses "short circuit" the normal pathway and travel across the heart in an abnormal way. Abnormal pathways or routes for the impulses can develop, causing irregularities in the heartbeat, or arrhythmias. In other cases, arrhythmias arise when areas other than the sinus node become active and begin to send out impulses that either compete with or take over the pacemaker function of the sinus node. Typically, the result of these abnormalities is a heartbeat that is too fast or too low. This may develop in any location within the atria, or ventricles. When the fast rhythm involves tissue from the upper part of the heart, it is known as supraventricular tachycardia. When it involves tissue from the lower chambers only, it is known as ventricular tachycardia.

Cardiac arrhythmia is any of a group of conditions in which the electrical activity of the heart is irregular, faster or slower than normal. The heartbeat may in fact be too fast or too slow or may follow an irregular rhythm. A heart beat that is too fast, by convention above 100 beats per minute in human adults, is called tachycardia, and a heart beat that is too slow, conventionally below 60 beats per minute, is called bradycardia. [Mandel, 1995]

2.1.2 RFA as Cardiac Arrhythmia Treatment

Treatment of cardiac arrhythmias consists in the removal of undesired tissues, which can be performed by several methods with various degrees of sophistication such as conventional surgery, electrosurgery, cryosurgery, laser and even high-intensity acoustic waves. These techniques offer advantages and disadvantages in terms of safety, controllability and side-effects. The choice of the surgeon is therefore a trade-off between the nature of the intervention, the risks and complications and the equipment availability and personal experience.

In some cases, the treatment of arrhythmias consists in destroying (ablating) internal heart tissues. These procedures, also called catheter techniques present interesting advantages because they eliminate the need for open chest surgery.

Radio-frequency ablation involves the generation of heat by the flow of an alternative current through the tissue to be ablated. In current practice, high frequency alternating current (350-500 kHz) RF ablation is used. This is preferred over previously used low frequency AC or DC pulses, as no directly stimulation of the heart muscle is produced, and therefore general anesthesia is not required.

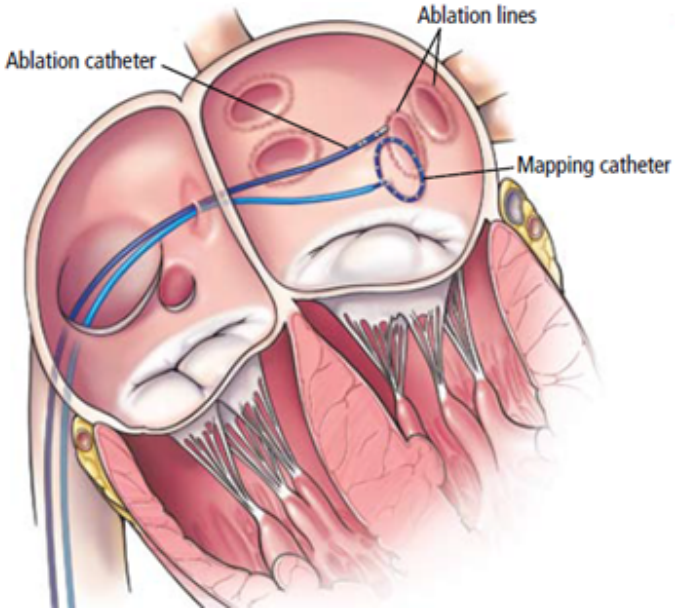

FIGURE 2.1: Pulmonary Radio-frequency ablation procedure.©Cleveland Clinic Journal of Medicine, 2009. 76(9):545.

2.2 Radio-frequency Ablation Temperature Modeling

As mentioned before, RFA of tissue is becoming more frequently used for therapy of several types of cardiac arrhythmia. RF catheter ablation is a technique whereby currents with frequencies between 300 kHz and 500 kHz are applied through electrodes to tissue. Tissue in the immediate vicinity of the electrode is heated based upon the Joule effect, whereas at farther locations its temperature is increased mainly by thermal conduction. The region heated above $\approx 50\,^{\circ}$C C becomes irreversible damaged and defines the lesion volume.

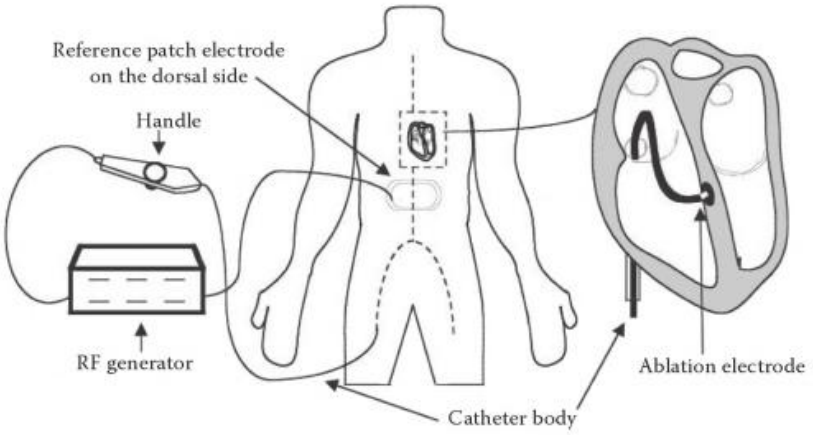

FIGURE 2.2: Positioning of the ablation catheter in a heart chamber. The ablation electrode, carried at the distal tip of the catheter, is connected to an RF generator that delivers the energy required by the particular therapy. [Panescu et al., 1995]

To be therapeutically effective, the ablation must be performed in a volume confined to the targeted region so that undesired tissue damage is avoided. This is a difficult goal to achieve since the optimal lesion geometries vary with the disease.

In order to avoid charring and tissue micro-explosions, it is of necessity to control the tissue temperature not to exceed 100 °C. We have also to take into account that, due to temperature gradients, the temperature sensors incorporated in ablation catheters usually do not measure precisely the highest temperature of the tissue. Therefore, it is useful to study how the current density and the temperature are distributed around the ablation electrodes.

2.2.1 Radio-frequency Heating Process

The change in temperature during ablation at any point in the tissue is given by the heat transfer equation called 'Modified Pennes Bioheat Equation' [Panescu et al., 1995]

$$\rho c \frac{\partial T}{\partial t} = \nabla \cdot k \nabla T + \mathbf{JE} - h_{bl}(T - T_{bl}) - Q_{el} \tag{2.1}$$
$$h_{bl} = \rho_{bl} c_{bl} w_{bl} \ ,$$

where ρ is the mass density, c is the heat capacity, k is the thermal conductivity, $\mathbf{J}$ is the current density, $\mathbf{E}$ is the intensity of the electric field, ρ_{bl} is the blood density, c_{bl} is the blood heat capacity, w_{bl} is the blood perfusion, T_{bl} is the blood temperature, and Q_{el} accounts for the heat exchanged between the tissue and the ablation electrode. Q_{el} is usually is negligible. However, it becomes an important parameter in the design of actively cooled ablation electrodes.

RFA probes operate between 350-550 kHz. At these frequencies, the wavelength of the electromagnetic energy is several orders of magnitude larger than the size of the ablation electrodes. Thus, the primary mode of energy transfer is through electrical conduction and can be modeled as a coupled quasi-static electrical conduction and heat conduction problem. The current density and the electric field intensity can be computed from the Laplace equation as [Chang and Nguyen, 2004]

$$\nabla \cdot \sigma(T) \nabla V = 0 \ , \tag{2.2}$$

where ∇ is the gradient operator, $\sigma(T)$ is the temperature-dependent conductivity (Siemens/meter), and V is the electric potential (Volts).

2.3 Optoacoustic Imaging

Optoacoustic (OA) imaging, also called photoacoustic imaging, has emerged in the last decade as a new biomedical imaging modality based on laser-generated ultrasound. This technique presents important advantages derived from the combination of the high-contrast of optical imaging and the high spatial resolution of ultrasound (US) imaging. An OA image can be regarded as an ultrasound image

in which the contrast is given by the optical properties of tissues, specifically optical absorption. This leads to higher contrast specificity than in conventional US imaging and to greater penetration depth than in purely optical imaging based on ballistic photons. Another difference with respect to US imaging is that US scanners produce focal peaks pressures that exceed 1 MPa, whereas OA amplitudes are typically lower than 10 kPa. Thereby, considering that light exposure is non-ionizing and the excited ultrasound waves are very weak, there are not major concerns regarding the safety of OA imaging. These attributes lend OA imaging to a wide variety of applications in clinical medicine, preclinical research and basic biology for studying cancer, cardiovascular diseases, abnormalities of the microcirculation and other conditions.

OA imaging works with the formation of ultrasound waves by irradiating tissue with electromagnetic radiation. Typically, optical wavelengths in the near-infrared (NIR) range (650-900 nm) are used in order to minimize optical absorption in tissue chromophores, which leads to a higher penetration depth. Thermoacoustic imaging can even reach deeper locations by employing longer wavelengths (frequencies of 300MHz-3GHz) in the elctromagnetic spectrum. OA imaging provides high-contrast imaging o fvascular structures, which can be hard to visualize with pulse-echo US. However, this comes at the expense of a lower penetration depth, which is mainly determined by the attenuation of light. The strong spectral discrimination of OA imaging also allows to identify specific absorbing substances such as oxygenated and deoxygenated hemoglobin as well as a large variety of extrinsically-administered contrast agents. Thereby, OA is also promising for functional and molecular imaging applications.

For short-pulse excitation, the optoacoustically-generated acoustic pressure $p(\vec{r}, t)$ in an acoustically homogeneous inviscid medium is given by [Cox and Beard, 2004]

$$\nabla^2 p(\vec{r}, t) - \frac{1}{c_s^2} \frac{\partial^2}{\partial t^2} p(\vec{r}, t) = -\frac{\beta}{C_p} \frac{\partial}{\partial t} \Theta(\vec{r}, t) \ , \tag{2.3}$$

where c_s is the speed of sound in medium, β is the thermal expansion coefficient, and C_p is the specific heat capacity at constant pressure. Θ is the heating function, representing the amount of energy absorbed in the tissue per unit volume and unit time. Eq.2.3 is valid under thermal confinement conditions, which ensure that heat conduction is negligible during the laser pulse excitation. Thermal confinement is guaranteed when the duration of the laser pulse is much shorter than the thermal relaxation time. The forward solution to Eq. 2.3 is given by [Cox and Beard, 2004]

$$p(\vec{r},t) = \frac{\beta}{4\pi C_p}\int \frac{d\vec{r'}}{|\vec{r}-\vec{r'}|}\frac{\partial\Theta(\vec{r'},t')}{\partial t'}\bigg|_{t'=t-|\vec{r}-\vec{r'}|/c_s} . \tag{2.4}$$

In case the temporal variation of the light source can be modeled as a Dirac's delta, Eq. 2.4 can be further simplify to

$$p(\vec{r},t) = \frac{1}{4\pi c_s^2}\frac{\partial}{\partial t}\left[\frac{1}{c_s t}\int d\vec{r'} p_0(\vec{r'})\delta\left(t-\frac{|\vec{r}-\vec{r'}|}{c_s}\right)\right] . \tag{2.5}$$

2.3.1 Optoacoustic Image Contrast

When the surface of the tissue is illuminated with a laser pulse, light undergoes two different types of phenomena, namely scattering and absorption. Absorption takes place at specific molecules called chromophores. The absorbed electromagnetic energy is then converted into heat by vibrational and collisional relaxation, which in turn induces acoustic pressure due to an increase in the volume of the tissue. The contrast mechanism is then given by an optically induced initial pressure p_0. The initial pressure distribution p_0 is encoded onto a propagating acoustic wave which, upon detection by an ultrasound transducer, is converted to a time-resolved electrical signal. Since the OA image is formed from a set of such OA signals detected at different spatial points, it follows that the OA image is a representation of p_0. p_0 is related to the heating produced by the deposited laser energy. If impulsive heating is assumed, the acoustic propagation time is small compared with the length scale of the heated volume. Then, by simple thermodynamic considerations it can be shown that p_0 at point r is proportion is proportional to

the Grüneisen parameter Γ and the absorbed optical energy per unit volume $H(r)$ [Cox and Beard, 2005]

$$p_0(r) = \Gamma H(r) \ , \tag{2.6}$$

where

$$\Gamma = \beta c_s^2 / C_p \ , \tag{2.7}$$

and $H(r)$ is the absorbed energy per unit volume given by

$$H(r) = \mu_a(r)\phi(r, \mu_a, \mu_s, g) \ . \tag{2.8}$$

Therefore, $p_0(r)$ is proportional to the product of $\mu_a(r)$ and the fluence ϕ which is itself dependent on $\mu_a(r)$. p_0 thus depends nonlinearly on $\mu_a(r)$ as

$$p_0(r) = \Gamma \mu_a \phi(r, \mu_a, \mu_s, g) \ . \tag{2.9}$$

$p_0(r)$ depends upon a variety of mechanical, thermodynamic and optical parameters. However, the changes in mechanical and thermodynamic properties for different tissue types are usually considered to be significant as compared to changes in optical absorption, and then they are typically regarded as being spatially invariant. There are inevitably some limits to this assumption and in some cases that image contrast provided by certain tissues may in part originate from the heterogeneities in the Grüneisen coefficient. However, generally image contrast can be assumed to be dominated by the optical absorption of the tissue.

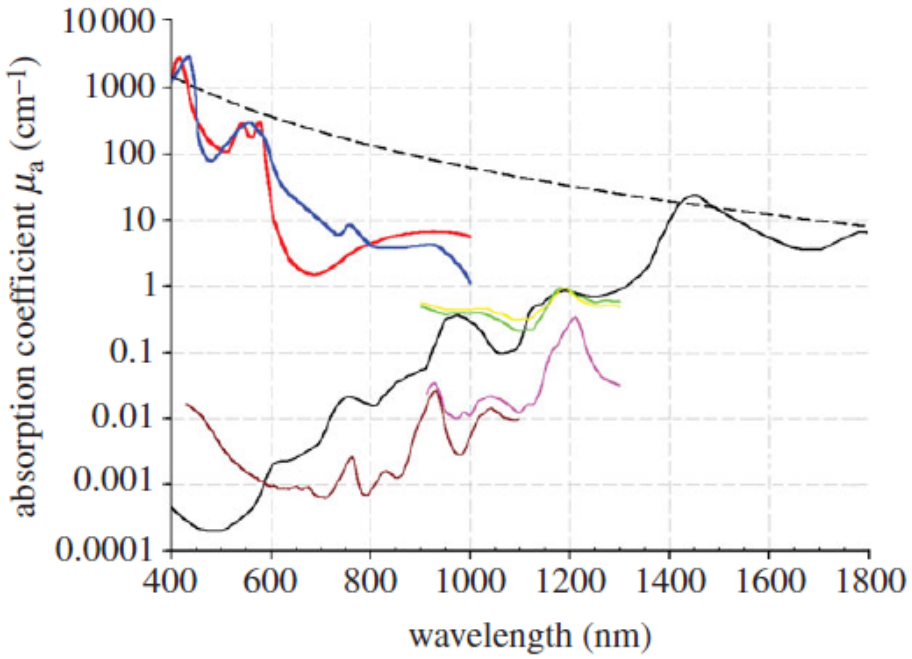

FIGURE 2.3: Absorption coefficient spectra of endogenous tissue chromophores.Absorption coefficient spectra of endogenous tissue chromophores. Oxyhaemoglobin (HbO_2), red line. Deoxyhaemoglobin (Hb), blue line. Water, blackline(80 % by volume in tissue). Lipid, brown line(20 % by volume in tissue). Lipid, pink line. Melanin, black dashed line, μ_a corresponds to that in skin). Collagen, green line and Elastin, yellow line [Beard, 2011]

The dominance of optical absorption as the primary source of OA image contrast implies that OA imaging is suitable for the visualization of anatomical features that contain an abundance of chromophores such as hemoglobin, lipids and water. Of these, hemoglobin is the most important for wavelengths below 1000 nm. As Figure 2.3 shows, between 650 and 900 nm the absorption coefficients of both the oxygenated (HbO_2) and deoxygenated (Hb) states of hemoglobin at physiologically realistic concentrations are at least an order of magnitude higher than the other major chromophores, such as water, lipids and elastin that are present in connective tissues, blood vessels and other organ constituents. At shorter wavelengths corresponding to the visible part of the spectrum, hemoglobin absorption is even higher and can exceed that of other chromophores by more than two orders of magnitude. It is the very strong preferential absorption of hemoglobin that enables the vasculature to be visualized with such high contrast in OA images.

Furthermore, the differences in the absorption spectra of HbO_2 and Hb shown in Figure 2.3 can be exploited to measure blood oxygenation by acquiring images at multiple wavelengths and applying spectroscopic analysis. In this way, the absorption-based contrast of OA imaging allows functional as well as structural images of the vasculature to be obtained.

Although melanin has a higher absorption coefficient than blood, it tends to be highly localized in regions such as the skin or the retina rather than being a major constituent of most tissues. It does not therefore tend to dominate OA image contrast in the way that hemoglobin does. Nevertheless, it forms an important source of contrast for visualizing melanin-rich structures such as certain pigmented lesions in the skin and the retinal-pigmented epithelium (RPE). Absorption by lipids is significantly lower than that of hemoglobin over the visible and NIR range up until around 1100 nm when blood absorption is dominated by water rather than hemoglobin and the strong lipid absorption peak at 1210 nm becomes predominant. This peak can be exploited to image localized lipid deposits. Chromophores such as hemoglobin and melanin absorb much more strongly than other tissue chromophores and thus provide an obvious source of primary contrast. However, although the more weakly absorbing chromophores such as water and lipids which may not be obviously visible on an OA image, they can still be detected by exploiting their characteristic spectral signatures. [Beard, 2011]

2.3.2 Penetration Depth

Penetration depth is ultimately limited by optical and acoustic attenuation. In general, for most soft tissues and at standard ultrasound frequencies, although acoustic attenuation can be significant, it is optical attenuation that dominates. Optical attenuation depends on both the absorption and scattering coefficients and is strongly wavelength-dependent. [Tsai et al., 2001]

In optically scattering media such as tissues, the optical penetration depth is best characterized by the effective attenuation coefficient μ_{eff} derived from diffusion theory, where

$$\mu_{eff} = (3\mu_a(\mu_a + \mu_s))^{1/2} \ . \tag{2.10}$$

In a homogeneous scattering media, light becomes diffusive for depths beyond several transport mean free paths (approx. 1mm) and the irradiance decays exponentially with depth with μ_{eff} the exponential constant. $1/\mu_{eff}$ therefore represents the depth at which the irradiance has decreased by $1/e$ and regarded as the penetration depth. Beyond the first millimeter in tissue, light is attenuated by approximately an order of magnitude for each additional centimeter of penetration depth. [Beard, 2011]. This represents one of the major challenges in OA imaging as imaging for several centimeters within tissue implies a signal attenuation of several orders of magnitude, so that extremely weak (undetectable) ultrasound signals are excited. Despite this fact, through careful choice of wavelength, optimization of the light delivery, transducer design parameters and signal processing, it has been demonstrated that penetration depths of several centimeters are attainable. A penetration depth of 4 cm has been achieved *in vivo* in the human breast [Kruger et al., 2010] using an excitation wavelength of 800 nm. Other studies using tissue phantoms and *ex vivo* tissues have suggested that depths of 5-6 cm may be achievable with the use of contrast agents [Ku and Wang, 2005]. With regard to the optimum wavelength range, it has been suggested that longer wavelengths, such as 1064 nm, at which blood absorption is low, might provide a penetration depth advantage if contrast agents that absorb at this wavelength are used [Homan et al., 2010].

2.3.3 Spatial Resolution

In common with pulse-echo US imaging, spatial resolution depends ultimately on the frequency content of the acoustic wave arriving at the detector. In OA

imaging, nanosecond excitation laser pulses are most often used and can result in extremely broadband acoustic waves with a frequency content extending to several tens or even hundreds of Megahertz, depending on the length scale of the optical absorbers. Under these conditions, the bandwidth of the OA signal and thus the spatial resolution is not usually limited by the generation process itself. Instead, it is the band-limiting acoustic attenuation OA waves that limits the maximum frequency content of the OA wave and thus defines the ultimate practically achievable spatial resolution limit. Under these circumstances, spatial resolution scales with depth. Acoustic attenuation strongly depends upon tissue type but an approximate rule of thumb is that for centimeter penetration depths, sub-millimeter spatial resolution is possible, decreasing to sub-100μm for millimeter penetration depth and sub-10μm spatial resolution for depths of a few hundred micrometers. Although acoustic attenuation defines the ultimate spatial resolution limit, other factors such as detector bandwidth, element size and the area over which the OA signals are recorded — the detection aperture — can be limiting factors in practice. This factors are particularly relevant when imaging superficial features that lie within a few millimeters of the surface. The bandwidth of the OA signal can then extend to several tens of megahertz presenting significant challenges in terms of meeting the detection bandwidth and spatial sampling requirements. For very small penetration depths (less than 1 mm), the focused light beam is still not significantly distorted by optical scattering and, the lateral resolution is limited by optical diffraction. Optical diffraction depends on the optical wavelength and the numerical aperture (NA) of the focusing lens and can be as small as few micrometers. Vertical resolution, however, remains limited by acoustic attenuation.[Beard, 2011]

2.4 Monitoring of Tissue Temperature Dependence

Non-invasive real-time measurement of temperature during ablation is necessary for the safe and efficient thermal destruction of tumors or other abnormal tissues.[Lehmann 1990, Welch and van Gemert 1995].

One of the potential applications of OA imaging is to be used for non-invasive, real-time temperature monitoring during ablation. In this way, OA imaging can potentially be used to improve the safety and efficacy of thermal therapy by predicting unwanted damage. For this, accurate temperature maps should provide the necessary control to minimize thermal tissue damage.

The thermal expansion of an absorbing medium heated by a short laser pulse with an incident laser fluence, ϕ_0, induces a pressure rise, $P(z)$, in the irradiated volume upon stress-confined irradiation conditions [Gusev and Karabutov, 1993a].

It is known that the Grüneisen parameter of water is temperature dependent (Fig. 2.4). This study demonstrated the linear dependence of the OA pressure amplitude on temperature in water and, thus, can be expressed by an empirical equation. For biological tissues, the Grüneisen parameter is also temperature-dependent and can be empirically approximated as [Wang and Wu, 2007]

$$\Gamma_w\left(T_0\right) = 0.0043 + 0.0053T_0 \ , \tag{2.11}$$

where T_0 is the temperature in degrees Celsius.

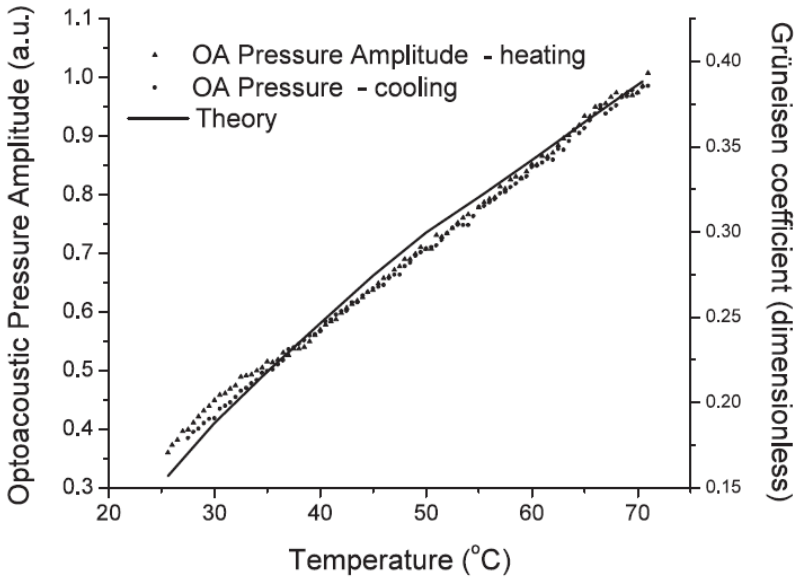

FIGURE 2.4: Theoretically calculated water Grüneisen coefficient and optoacoustic pressure amplitude induced in aqueous solution as a function of temperature. [Larina et al., 2005]

On the other hand, the optical absorption and scattering coefficients and hence the optical attenuation may also have a temperature dependence, particularly if heating leads to chemical transformation in the tissue.

Therefore, by recording and analyzing the OA pressure profile in time, it is expected that one can reconstruct the temperature distribution during hyperthermia occurred in ablation processes.

Chapter 3

Thermal Modeling

To demonstrate the OA imaging capabilities in temperature monitoring during ablation, we first studied how the OA signal behaves under temperature changes. OA signals change in areas where the tissue has been damaged, coagulated, or heated but still undamaged. Indeed, the Grüneisen parameter increases significantly with temperature. Moreover, the speed of sound also increases with temperature. When the tissue temperature during RFA goes beyond 50°C, irreversible changes that affect electrical tissue properties take place. These irreversible changes, such as coagulation, are mainly due to changes at the cellular level of cell membrane properties and dehydration resulting in a permanent increase in electrical conductivity.

Therefore, OA signals from the treated tissue area provide a very valuable feedback on the tissue properties. These properties are related to the tissue coagulation level (which is associated to its optical absorption) and temperature. Decoupling these parameters, optical absorption and temperature, such that both can be measured during the heating process requires developing an accurate thermal heating model of the ablation process. Coupling the latter thermal model to a temperature-dependent OA model will enable to predict the tissue temperature from the OA signal.

Accurate measurement of the temperature is important in an ablation process to predict unwanted damage. Even if we may be able to notice damage with image

guidance methods, these visual methods give feedback of the damage once it is done. Keeping track of tissue temperature we could avoid damage in undesired areas. Moreover, knowing the temperature allows properly correcting for speed of sound variations and thus make better images reconstructions.

The strategy followed in this work, as this chapter is structured, was first to develop a thermal model for a general transient heating process, and secondly model the radio-frequency heating process case.

3.1 Modeling Conductive Heating

The problem of solving a conductive-convective heating process case, such as agarose solution phantoms being heated by an air heat flux, is addressed in this section. We introduce the existing heat transfer theories and explain which one will be used in our studies and why.

3.1.1 Conduction Model Solution Approaches

3.1.1.1 Steady State Heating Processes

Heat transfer due to convection involves the energy exchange between a surface and an adjacent fluid. A distinction must be made between forced convection, wherein a fluid is made to flow past a solid surface by an external agent such as a fan or pump, and free or natural convection wherein a warmer (or cooler) fluid next to the solid boundary causes circulation because of a difference in density resulting from the temperature variation throughout a region of the fluid.

The rate equation for convective heat transfer was first expressed by Newton in 1701, and is referred to as the Newton rate equation.

$$\frac{q}{A} = h \cdot \Delta T \ , \tag{3.1}$$

where q is the rate of convective heat transfer, in W or Btu/h. A is the area normal to the heat flux direction in m^2 or ft^2. ΔT is the temperature difference between surface and fluid in °K and h is the convective heat transfer coefficient, in $W/(m^2{\cdot}°\mathrm{K})$ or $Btu/(h{\cdot}ft^2{\cdot}°\mathrm{K})$.

Steady-state heat conduction implies that temperature and heat flow at each point do not change with time. Fig. 3.1 depicts an example of steady-state conduction through a plane wall with its surfaces held at constant temperatures $T1$ and $T2$.

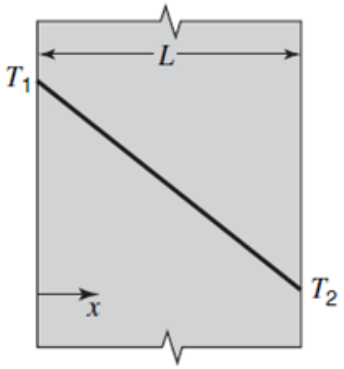

FIGURE 3.1: Steady-state conduction through a plane wall.[Welty et al., 2007]

The Fourier rate equation, derivative form of Newtons Eq. 3.1, for the x direction is given by

$$\frac{q_x}{A} = -k\frac{dT}{dx} \ . \tag{3.2}$$

Solving Eq.3.2 for q_x subject to the boundary conditions $T = T_1$ at $x = 0$ and $T = T_2$ at $x = L$ it results

$$\frac{q_x}{A}\int_0^L dx = -k\int_{T1}^{T2} dT = k\int_{T2}^{T1} dT \ . \tag{3.3}$$

Then the net heat flux going into the slab, this is, the incoming heat flux less the outgoing heat flux, is calculated as

$$q_x = \frac{kA}{L}(T_1 - T_2) \ . \tag{3.4}$$

If the heating process were steady-state, the procedure to solve the thermal profile would be as follows

$$q_{in}(t) - q_{out}(t) = q_0(t) = \frac{kA}{L}(T_S(t) - T_0(t)) \ . \tag{3.5}$$

Thereby if we adjust the heat flux so $q_0(t)$ is constant and we have thermocouples to measure $T_s(t)$ and $T_0(t)$, then from Eq.3.5 we could compute the value of $q_0(t)$.

The thermal profile described across the phantom will have a certain temperature depending on the distance from the heated wall (x) and time (t), that is, $T(x,t)$.

$$T(x,t) = T_S(t) - \frac{\left[\frac{kA}{L}(T_S(t) - T_0(t))\right] \cdot x}{k \cdot A} \ . \tag{3.6}$$

3.1.1.2 Transient Heating Processes: Analytical Method

Transient conduction occurs when the temperature within an object changes as a function of time. Analysis of transient systems is more complex and often requires the application of approximation theories(Analytical Methods) or numerical analysis by computer(Numerical Methods). In this subsection we present the analytical solution approximation that is described in Çengel's book [A.Çengel, 2006].

A semi-infinite solid is an idealized body that has a single plane surface and extends to infinity in all directions, as shown in Fig.3.2

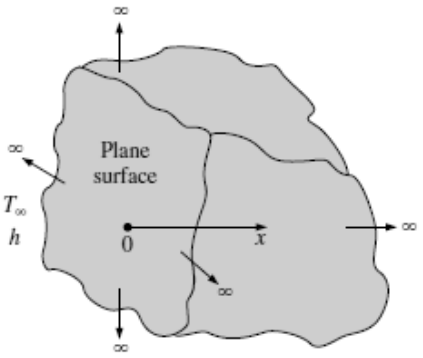

FIGURE 3.2: Schematic of a semi-infinite body.[A.Çengel, 2006]

This idealized body is used to indicate that the temperature change in the part of the body in which we are interested is due to thermal conditions on a single surface.

For shorts periods of time, most bodies can be modeled as semi-infinite solids since heat does not have sufficient time to penetrate deep into the body, and the thickness of the body does not enter into the heat transfer analysis. For example, a body whose surface is heated by a laser pulse can be treated as semi-infinite solid.

We assume a semi-infinite solid with constant thermophysical properties, no internal heat generation, uniform thermal conditions on its exposed surface, and an initial uniform temperature of T_i throughout the surface. Heat transfer in this case occurs only in the direction normal to the surface (the x direction), and thus it represents a one-dimensional problem. Differential equations are independent of the boundary or initial conditions, and thus one-dimensional transient conduction in Cartesian coordinates applies. The depth of the solid is large ($x \to \infty$) compared to the depth that heat can penetrate, and these phenomena can be expressed mathematically as a boundary condition as $T(x \to \infty, t) = T_i$.

Heat conduction in a semi-infinite solid is governed by the thermal conditions imposed on the exposed surface, and thus the solution depends strongly on the boundary condition at $x = 0$.

The governing equations of transient conduction are:

$$Differential\ equation \quad \frac{\partial^2 T}{\partial x^2} = \frac{1}{x}\frac{\partial T}{\partial t} \tag{3.7}$$

$$Boundary\ conditions \quad T(0,t) = T_S \ and \ T(x \to \infty, t) = T_i \tag{3.8}$$

$$Initial\ Condition \quad T(x,0) = T_i \ . \tag{3.9}$$

An approach converts the partial differential equation into an ordinary differential equation by combining the two independent variables x and t into a single variable

η called similarity variable.

$$Similarity\ variable \quad \eta = \frac{x}{\sqrt{4\alpha t}} \ . \tag{3.10}$$

Assuming $T = T(\eta)$ and using the chain rule, all derivatives in the heat conduction equation can be transformed into the new variable as

$$\frac{\partial^2 T}{\partial x^2} = \frac{1}{\alpha}\frac{\partial T}{\partial t} \text{ and } \eta = \frac{x}{\sqrt{4\alpha t}} \tag{3.11}$$

$$\frac{\partial T}{\partial t} = \frac{dT}{d\eta}\frac{\partial \eta}{\partial t} = \frac{x}{2t\sqrt{4\alpha t}}\frac{dT}{d\eta} \tag{3.12}$$

$$\frac{\partial T}{\partial x} = \frac{dT}{d\eta}\frac{\partial \eta}{\partial x} = \frac{1}{\sqrt{4\alpha t}}\frac{dT}{d\eta} \tag{3.13}$$

$$\frac{\partial^2 T}{\partial x^2} = \frac{d}{d\eta}\left(\frac{\partial T}{\partial x}\right)\frac{\partial \eta}{\partial x} = \frac{1}{4\alpha t}\frac{\partial^2 T}{\partial \eta^2} \ , \tag{3.14}$$

where $\eta = 0$ at $x = 0$ and $\eta \to \infty$, as well as in $t = 0$, then:

$$\frac{\partial^2 T}{\partial \eta^2} = -2\eta\frac{dT}{d\eta} \tag{3.15}$$

$$T(0) = T_S \text{ and } T(\eta \to \infty, t) = T_i \ . \tag{3.16}$$

The second boundary condition and the initial condition result in the same boundary condition. Both the transformed equation and the boundary conditions depend on η only and are independent of x and t. Therefore, the transformation is successful, and η is indeed a similarity variable.

To solve the second order ordinary differential Eq.3.15 a new variable $w = dT/d\eta$ needs to be defined. This reduces the equation into a first order differential equation than can be solved by separating variables as

$$\frac{\partial w}{\partial \eta} = -2\eta d\eta \to ln(w) = -\eta^2 + C_0 \ \to \ w = C_1 e^{-\eta^2} \ , \tag{3.17}$$

where $C_1 = lnC_0$. Back substituting $w = dT/d\eta$ and integrating again:

$$T = C_1 \int_0^{\eta} e^{-u^2} du + C_2 \ , \tag{3.18}$$

where u is an integration variable. The boundary condition at $\eta = 0$ gives $C_2 = T_S$, and for the one at $\eta \ \rightarrow \ \infty$ gives:

$$T_i = C_1 \int_0^{\infty} e^{-u^2} du + C_2 = C_1 \frac{\sqrt{\pi}}{2} + T_S \ \rightarrow \ C_1 = \frac{2(T_i - T_S)}{\sqrt{\pi}} \ . \tag{3.19}$$

Substituting the C_1 and C_2 expressions into Eq.3.18 and rearranging, the variation of temperature is then given by

$$\frac{T - T_S}{T_i - T_S} = \frac{2}{\sqrt{\pi}} \int_0^{\eta} e^{-u^2} du = erf(\eta) = 1 - erfc(\eta) \ , \tag{3.20}$$

where the mathematical functions $erf(\eta)$ and $erfc(\eta)$ are called the error function and the complementary error function, respectively, of argument η (Fig.3.3).

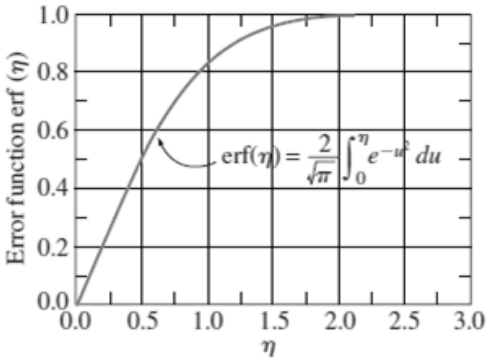

FIGURE 3.3: Error function is a standard mathematical function, just like the sinus and tangent functions, whose value varies between 0 and 1.

Despite the simple appearance, the integral in the definition of the error function cannot be performed analytically. Therefore, the function $erfc(\eta)$ is evaluated numerically for different values of η, and the results are listed in Table 3.4:

η	erfc (η)	η	erfc (η)	η	erfc (η)	η	erfc (η)	η	erfc (η)	η	erfc (η)
0.00	1.00000	0.38	0.5910	0.76	0.2825	1.14	0.1069	1.52	0.03159	1.90	0.00721
0.02	0.9774	0.40	0.5716	0.78	0.2700	1.16	0.10090	1.54	0.02941	1.92	0.00662
0.04	0.9549	0.42	0.5525	0.80	0.2579	1.18	0.09516	1.56	0.02737	1.94	0.00608
0.06	0.9324	0.44	0.5338	0.82	0.2462	1.20	0.08969	1.58	0.02545	1.96	0.00557
0.08	0.9099	0.46	0.5153	0.84	0.2349	1.22	0.08447	1.60	0.02365	1.98	0.00511
0.10	0.8875	0.48	0.4973	0.86	0.2239	1.24	0.07950	1.62	0.02196	2.00	0.00468
0.12	0.8652	0.50	0.4795	0.88	0.2133	1.26	0.07476	1.64	0.02038	2.10	0.00298
0.14	0.8431	0.52	0.4621	0.90	0.2031	1.28	0.07027	1.66	0.01890	2.20	0.00186
0.16	0.8210	0.54	0.4451	0.92	0.1932	1.30	0.06599	1.68	0.01751	2.30	0.00114
0.18	0.7991	0.56	0.4284	0.94	0.1837	1.32	0.06194	1.70	0.01612	2.40	0.00069
0.20	0.7773	0.58	0.4121	0.96	0.1746	1.34	0.05809	1.72	0.01500	2.50	0.00041
0.22	0.7557	0.60	0.3961	0.98	0.1658	1.36	0.05444	1.74	0.01387	2.60	0.00024
0.24	0.7343	0.62	0.3806	1.00	0.1573	1.38	0.05098	1.76	0.01281	2.70	0.00013
0.26	0.7131	0.64	0.3654	1.02	0.1492	1.40	0.04772	1.78	0.01183	2.80	0.00008
0.28	0.6921	0.66	0.3506	1.04	0.1413	1.42	0.04462	1.80	0.01091	2.90	0.00004
0.30	0.6714	0.68	0.3362	1.06	0.1339	1.44	0.04170	1.82	0.01006	3.00	0.00002
0.32	0.6509	0.70	0.3222	1.08	0.1267	1.46	0.03895	1.84	0.00926	3.20	0.00001
0.34	0.6306	0.72	0.3086	1.10	0.1198	1.48	0.03635	1.86	0.00853	3.40	0.00000
0.36	0.6107	0.74	0.2953	1.12	0.1132	1.50	0.03390	1.88	0.00784	3.60	0.00000

FIGURE 3.4: Complementary error function.

Knowing the temperature of the surface as a function of time will allows determining the heat flux at the surface using Fourier law, i.e

$$\dot{q}_S = -k\frac{\partial T}{\partial x}\Big|_{x=0} = -k\frac{dT}{d\eta}\frac{\partial \eta}{\partial x}\Big|_{\eta=0} = -kC_1 e^{-\eta^2}\frac{1}{\sqrt{4\alpha t}}\Big|_{\eta=0} = \frac{k(T_S - T_i)}{\sqrt{\pi \alpha t}} \ . \quad (3.21)$$

Solutions of Eq. 3.21 correspond to the case when the temperature of the exposed surface of the medium is suddenly raised to T_x at $t = 0$ and is maintained at that value at all times. Using a similar approach or the Laplace transform technique, analytical solutions can be obtained for other boundary conditions. The approach used in [A.Çengel, 2006] to obtain an analytical solution was considering a specified surface heat flux, $\dot{q}_S$ =constant. To use this method thus we must calculate the heat flux on the surface and take the average of its value in time (during the heating process). Once we have $\dot{q}_S(x = 0)$, we can apply the given analytical formula [A.Çengel, 2006]:

$$T(x,t) - T_i = \frac{\dot{q}_S}{k}\left[\sqrt{\frac{4\alpha t}{\pi}} exp\left(\frac{x^2}{4\alpha t}\right) - xerc\left(\frac{x}{2\sqrt{\alpha t}}\right)\right] \ . \quad (3.22)$$

3.1.1.3 Transient Heating Processes: Numerical Method

Finite-difference methods (FDM) are numerical methods for estimating the solutions to differential equations using finite difference equations to approximate derivatives. The governing differential equation for the conduction heating process presented is given by

$$Differential\ equation \quad \frac{\partial^2 T}{\partial x^2} = \frac{1}{\alpha}\frac{\partial T}{\partial t} \tag{3.23}$$

$$Boundary\ conditions \quad T(0,t) = T_S(t)\ and\ T(L,t) = T_i \tag{3.24}$$

$$Initial\ Condition \quad T(x,0) = T_i\ . \tag{3.25}$$

To use a finite difference method to approximate the solution to a problem, one must first discretize the problem's domain. This is usually done by dividing the domain into a uniform grid (Fig. 3.5). Therefore, finite-difference methods produce sets of discrete numerical approximations to the derivative in a "time-stepping" manner.

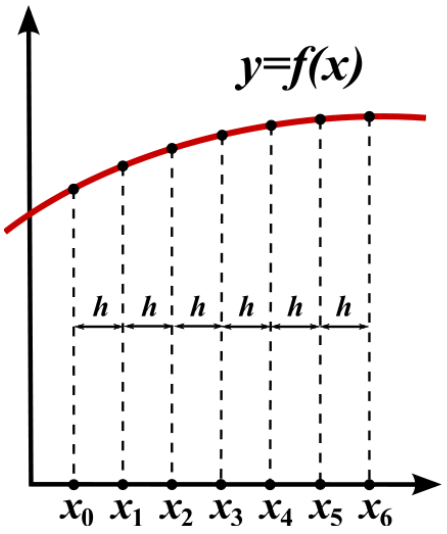

FIGURE 3.5: The finite difference method relies on discretizing a function on a grid. Retrieved from http://en.wikipedia.org/wiki/Finite_difference_method

There are several FDM methods depending of which stencil is used. Stencils represent the basic unit of the FDM. They correspond to the nodes of the grid that

is dicretized the domain in. The different methods to solve the heat conduction problem are:

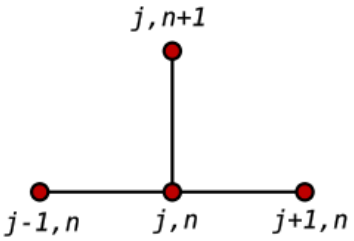

FIGURE 3.6: Forward in Time, Centered in Space (FTCS)

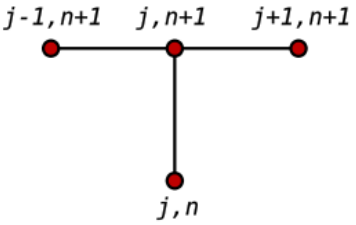

FIGURE 3.7: Backward in Time, Centered in Space (BTCS)

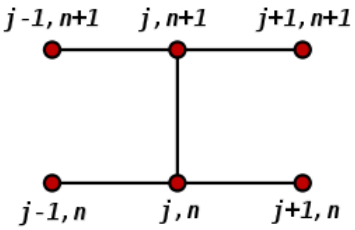

FIGURE 3.8: Crank-Nicolson

The FTCS method is the only one that has the possibility of becoming unstable and thus will have a stability condition(explained in section 3.1.4), whereas BTCS and Crank-Nicolson are always stable and thus will not have any stability condition. However, FTCS is less complex to implement in Matlab. BTCS and Crank-Nicolson FDM have more computational cost, being possibly necessary the implementation of LU factorization to the coefficients matrix in order to minimize the computational cost of the procedure.

3.1.1.4 Matlab Partial Differential Equation Tool

As a verification method for the analytical and the FDM methods solutions, we used Matlab partial differential (PDE) equation solver. Matlab PDE solver solves systems of parabolic and elliptic PDEs in one spatial variable x and time t.

Matlab PDE solver implemented in a function called pdepe, which calls other 3 functions; pdex1pde, pdex1ic and pdex1bc. Pdex1pde defines the coefficients of the PDE problem to solve in the syntax that Matlab requires. One must fit the formula into Matlab's form and write the adequate parameters for Matlab, in the following form

$$c\left(x,t,u,\frac{\delta u}{\delta x}\right)\frac{\delta u}{\delta t}=x^{-m}\frac{\delta}{\delta x}\left(x^{m}f\left(x,t,u,\frac{\delta u}{\delta t}\right)\right)+s\left(x,t,u,\frac{\delta u}{\delta x}\right)\ , \qquad (3.26)$$

where $f\left(x,t,u,\frac{\delta u}{\delta t}\right)$ is a flux term and $s\left(x,t,u,\frac{\delta u}{\delta x}\right)$ is a source term. The flux term must depend on $\delta u/\delta x$. The coupling of the partial derivatives with respect to time is restricted to multiplication by a diagonal matrix $c\left(x,t,u,\frac{\delta u}{\delta x}\right)$. The diagonal elements of this matrix are either identically zero or positive. An element that is identically zero corresponds to an elliptic equation and otherwise to a parabolic equation.

The second function called by pdepe function, pdex1ic, defines the initial conditions of our diffusion process to solve. At the initial time $t = t_0$, for all x the solution components satisfy initial conditions of the form:

$$u\left(x,t_0\right) = u_0\left(x\right) \ . \tag{3.27}$$

The last function called by pdepe function, pdex1bc, defines the boundary conditions of the system as

$$p\left(x,t,u\right) + q\left(x,t\right) f\left(x,t,u,\frac{\delta u}{\delta x}\right) = 0 \ , \tag{3.28}$$

where $q\left(x,t\right)$ is a diagonal matrix with elements that are either identically zero or never zero. The boundary conditions are expressed in terms of the f rather than partial derivative of u with respect to x $\frac{\delta u}{\delta x}$. Also, only coefficient p can depend on u.

3.1.2 Experimental Conductive Thermal Profile

In this subsection experimental thermal profiles to the conduction heating process are presented. In a second part, a description of these experimental data and a discussion of which approach should be taken is also treated.

We implemented several set-ups with phantoms of different sizes. For temperature measurements, we used 4 type-T thermocouples ordered to Physitemp Instruments Inc.(Clifton, New Jersey, USA). The set-up was made by putting the phantoms in

vertical position in front of the heat gun that was fixed to the table, at a distance of 30 cm. See Fig. 3.9.

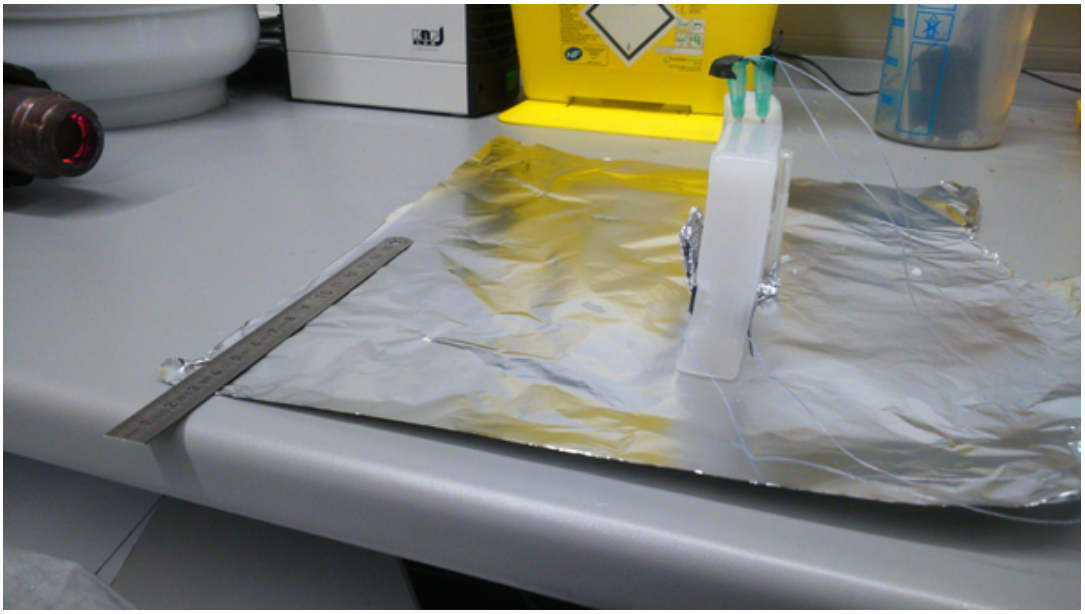

FIGURE 3.9: Broad view of the set-up including both, heat gun and phantom dispositions.

The first thermocouple (T1) and the last thermocouple (T4) were in contact with the heated surface and the back surface respectively using electrical tape, as shown in Fig.3.10. Whereas the thermocouples in the middle, T2 and T3, were introduced with needles inside to reach the center of the phantom, so the thermocouples' tips were describing a perpendicular line to phantoms' vertical surfaces.

The Data Acquisition System (DAQ) used in the experiments(Fig.3.10) is 'Thermes Usb'. It transforms the voltage coming form the thermocouples, due to their tip's temperature, into temperature values.

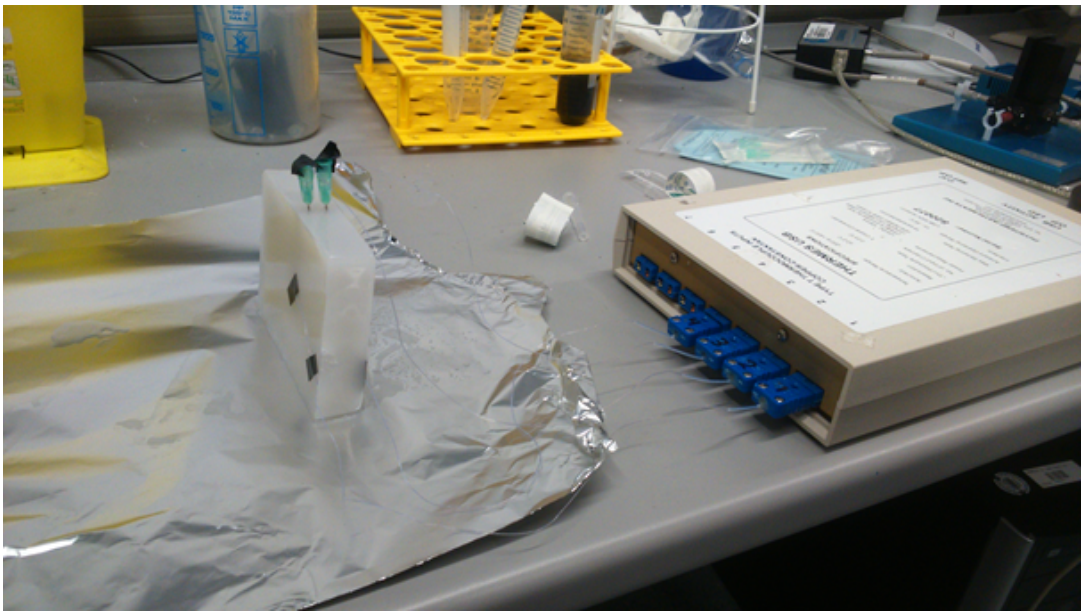

FIGURE 3.10: Thermocouples connected to DAQ 'Thermes Usb' (Physitemp)

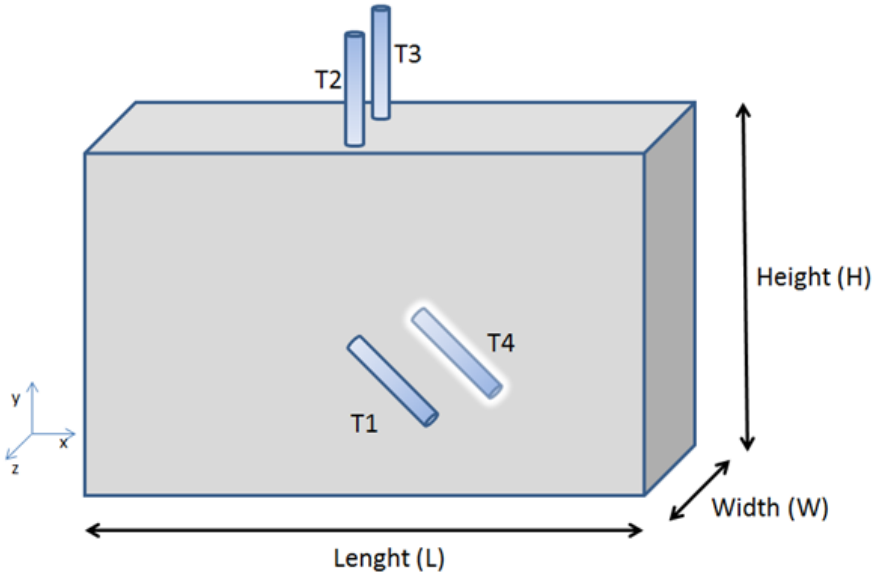

FIGURE 3.11: Phantom and placement of thermocouples scheme

Experiment Details

- The heat flux power of the heat gun was adjustable and it was fixed to level 9 during the entire heating process(1200seconds).,

- Neither the phantom or the heat gun moved their positions while the study was done.,
- Phantom's dimensions: Height=70mm,Width=18mm,Length=90mm.The phantom was created using 200 ml of de-ionized water and 2.860 g of agar. No Intralipid and no ink were added for this experiment because optical properties were not under study.,
- Thermocouples where positioned evenly within the thickness of the phantom describing a straight line, spaced 6mm from each other.(See Fig.3.11)

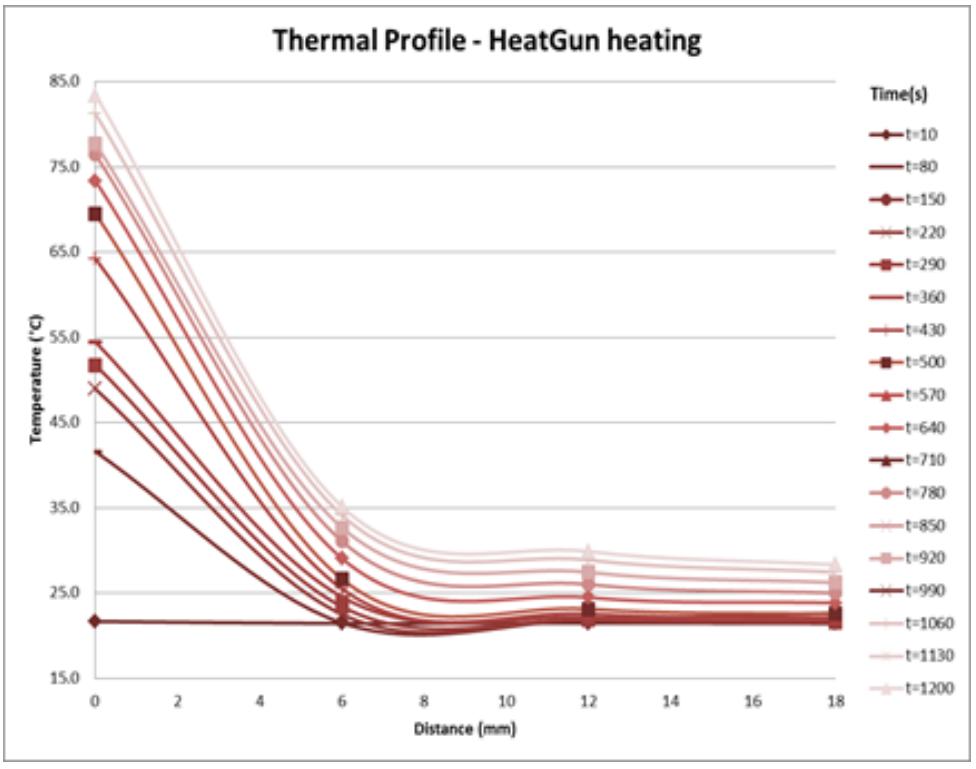

FIGURE 3.12: Conductive experimental Thermal Profile.

Experiment Conclusions

In order to simplify the thermal profile calculation, one may be to model it as a steady-state heating process. However the results shown in Fig. 3.12 clearly show that this is not possible.

It may be possible to approach a steady-state heat transfer by modifying the set-up to match the steady-state heat transfer conditions. However to approach a real process as an ideal process we should first review the properties and conditions of steady-state heat transfer processes.

The term steady implies no change with time at any position within the medium, while transient implies variation with time or time dependence. Therefore, the temperature or heat flux remains unchanged with time during steady heat transfer through a medium at any position of the heated medium, although both quantities may vary from one point to another.

During transient heat transfer, the temperature normally varies with time as well as position. In the special case of variation with time but no with position, the temperature of the medium changes uniformly with time for all points. Such heat transfer systems are called lumped systems. Most of heat transfer problems encountered in practice are transient in nature, but they are tried to be analyzed under steady conditions due to their simplicity. ([A.Çengel, 2006]). However, the conduction problem corresponding to a phantom being heated with a heat gun must be modelled as a transient heating processes.

The possibility of recreating a steady-state heating process modifying the set-up was discarded as. It might be highly time consuming and it would not have real applications due to the complex set-up that requires.

3.1.3 Conduction Heating Analytical Solution

From section 3.1.1.2 we have the analytical solving equation 3.22:

$$T(x,t) - T_i = \frac{\dot{q_S}}{k}\left[\sqrt{\frac{4\alpha t}{\pi}} exp\left(\frac{x^2}{4\alpha t}\right) - xerc\left(\frac{x}{2\sqrt{\alpha t}}\right)\right]. \qquad \text{(3.22 revisited)}$$

In an ablation process, the ablation catheter is the only instrument in contact with the tumor. Therefore, a thermocouple can be coupled to the tip of the catheter so that the tumor's surface temperature can be read in real time.

In the experiment of heating a phantom with the heat gun, the equivalent to the thermocouple placed in the catheter tip is the thermocouple on phantom's surface in the heat gun side (T_1). Therefore, T1 reading was used as the input for the thermal model.

T1 is measured on the surface of the phantom. This means that $x(T_1) = 0m$. For $x = 0m$ equation 3.22 is reduced to:

$$T(0,t) - T_i = \frac{\dot{q_S}}{k}\left[\sqrt{\frac{4\alpha t}{\pi}}\right] . \tag{3.29}$$

Having T1 temperature readings at different times we solved for the heat flux q_S by establishing $T(0,t) = T1(t)$ at every measurement instant. Measurements were taken every 10 seconds for a total of 1200 seconds, as shown in Figure 3.12. Therefore, the heat flux can be solved from the following equation:

$$\frac{(T(0,t) - T_i)k}{\sqrt{\frac{4\alpha t}{\pi}}} = \dot{q_S} = \frac{(T_1(t) - T_1(0))k}{\sqrt{\frac{4\alpha t}{\pi}}} . \tag{3.30}$$

Considering Eq.3.22 and taking the heat flux as the average of the heat flux during the heating process (in time), the analytical model predicted much higher temperatures in the positions of the thermocouples which could happen if extra heat is added into the phantoms. In the same way, on can interpret that the actual temperature results are lower than the theoretical ones because the heat absorbed by the phantoms was much lower than the one calculated for the model. In fact, the heat flux calculated for the model was the heat flux received by the surface of the phantom (it is based on T_1 readings). However, not all the heat heat was absorbed at the surface of the phantom, which would contribute to an increase in the phantom's temperature.

The amount of constant heat flux in time that gives the expected temperature predictions for all thermocouples in every phantom was $800W/m^2$. The latter amount represents 35% of the heat flux heating the surface of the phantom, which on average was $2500W/m^2$), so that only this percentage was absorbed.

Correcting for the heat flux absorbed by the phantom, T_2, T_3 and T_4 temperatures were modeled analytically. Thermocouples 2, 3 an 4 where positioned evenly within each phantom thickness. The analytical solution is plotted in Fig. 3.13.

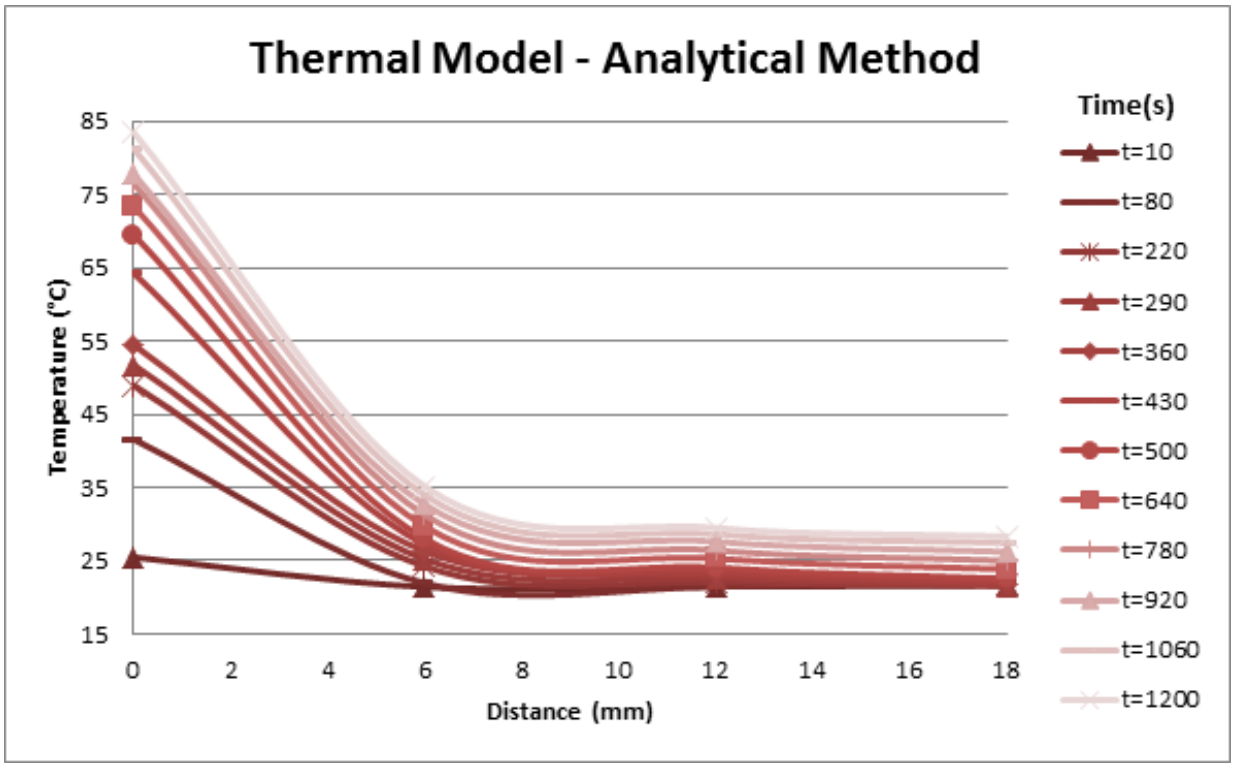

FIGURE 3.13: Analytical Solution Thermal Profile.

Comparing the experimental thermal profile shown in Fig.3.12 with the analytical solution shown in Fig. 3.13 one can appreciate that there is a good correlation between both thermal profiles.

In order to show the order of magnitude that we are working with, using this analytical solution, modeled temperatures for each thermocouple are compared in the next plots with their experimental values.

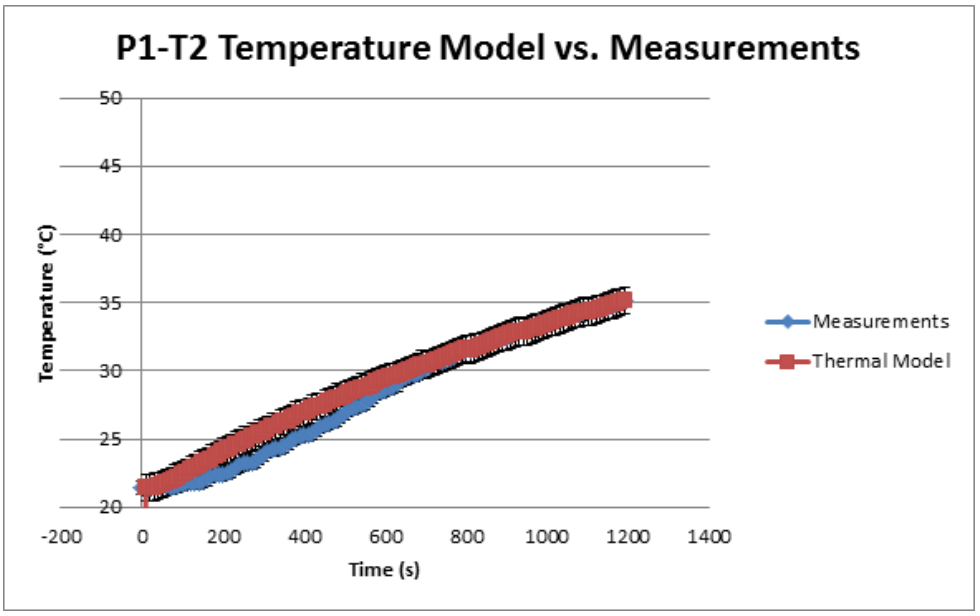

FIGURE 3.14: Modeled and measured values for T_2 in time.

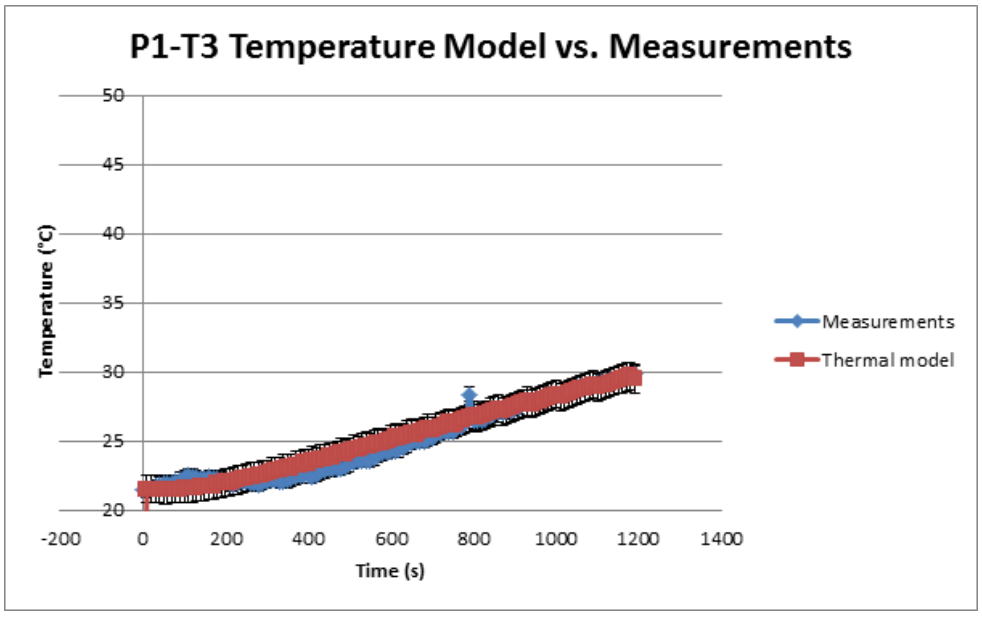

FIGURE 3.15: Modeled and measured values for T_3 in time.

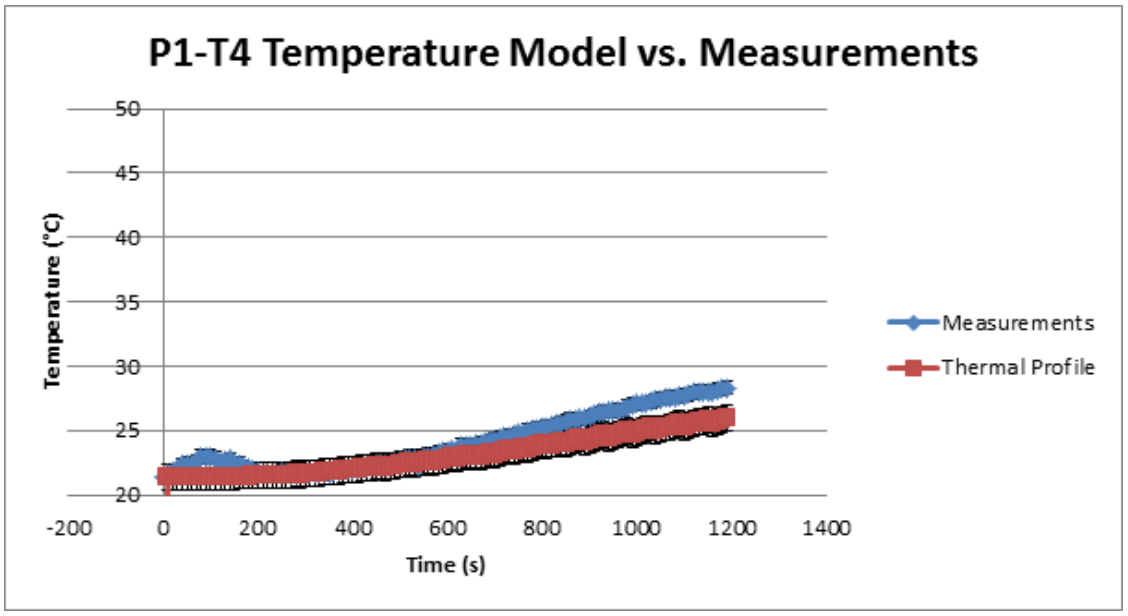

FIGURE 3.16: Modeled and measured values for T_4 in time.

As figures 3.14, 3.15 and 3.16 show the analytical solution approaches the expected values with an accuracy of $\pm 1°C$ in the worst case that is for T_4(Fig. 3.16).

3.1.4 Matlab Finite Difference Method

Solving the transient heat transfer case using the finite difference method (FDM) implemented in Matlab is a useful tool to be easily coupled with the already existing images reconstruction algorithms, correct their speed of sound value and thus improve the contrast of the images.

As every finite difference method we should start analyzing the governing equation and the initial and boundary conditions that are going to define our model.

$$Differential\ equation \quad \frac{\partial^2 T}{\partial x^2} = \frac{1}{\alpha}\frac{\partial T}{\partial t} \qquad \text{(3.23 revisited)}$$

$$Boundary\ conditions \quad T(0,t) = T_S(t)\ and\ T(L,t) = T_i \qquad (3.24)$$

$$Initial\ Condition \quad T(x,0) = T_i\ . \qquad (3.25)$$

where α is the thermal diffusivity in m^2/s, physical property of the medium. The starting point of the FDM method is our initial temperature condition $T(x,0) = T_i$ for every point of our discretized grid (Fig.3.17). For the rest of the time domain the FDM is constricted by the front and back surfaces. The temperature of the front surface is the reading of the thermocouple $T(0,t)$. Also, since during the ablation procedure there is only physical contact with the surface of the tissue, the back surface temperature is expected not to change and thus fixed to the initial value $T(L,t)$.

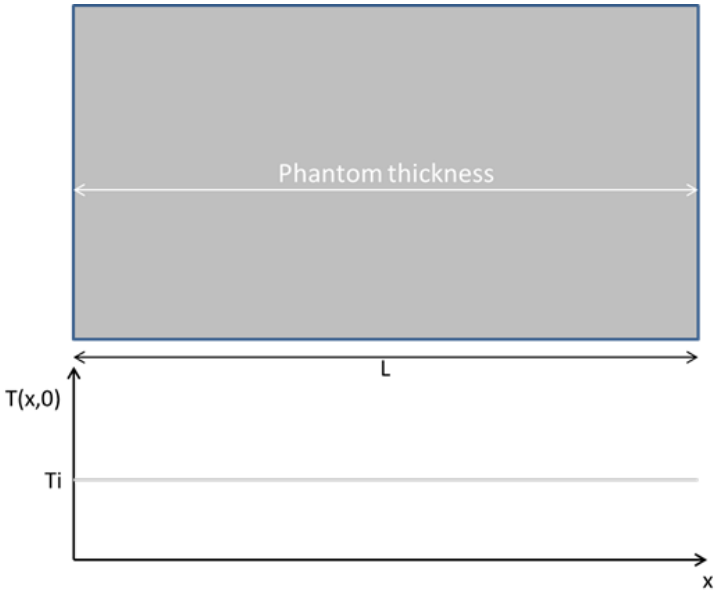

FIGURE 3.17: Initial temperature distribution $T(x,0) = T_i$.

The first step in the finite difference method is to construct a grid with the points of interest. Generally the discretization has a constant time step and is equally spaced as represented in Fig.3.18.

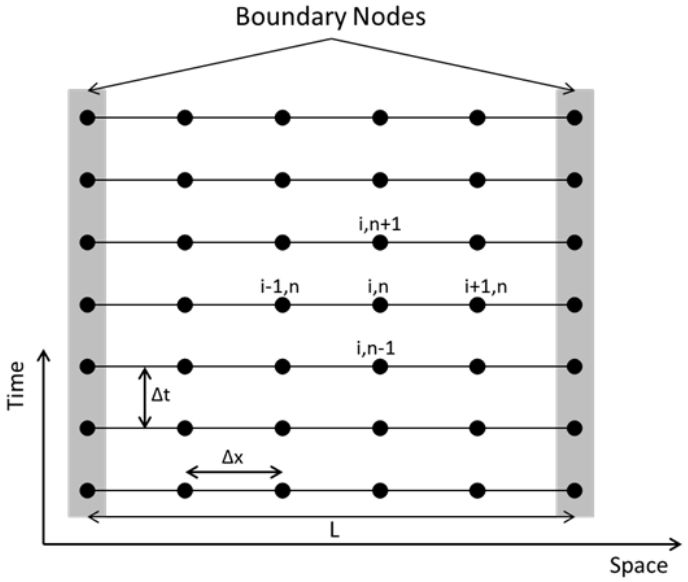

FIGURE 3.18: FDM grid discretization and nodes notation.

The next step is to replace the continuous derivatives of Eq.3.23 with their finite difference approximations. The implementation used was forward in time and centered in space (FTCS) because as it uses information from known nodes directly and thus has less computational cost. Using other methods, BTCS or Crank-Nickolson, the implementation of coefficient matrices and probably a LU factorization would be required to reduce computational cost.

The derivative of temperature versus time $\delta T/\delta t$ can be approximated with a FTCS scheme as:

$$\frac{\delta T}{\delta t} \approx \frac{T_i^{n+1} - T_i^n}{t^n + 1 - t^n} = \frac{T_i^{n+1} - T_i^n}{\Delta t} = \frac{T_i^{new} - T_i^{current}}{\Delta t} \ , \tag{3.31}$$

where n is the index for the temperature at the current time, $n+1$ the index for the temperature of the next time step. The subscript i refers to the location of the point in the discretized grid. Being n and i integers. The spatial derivative of Eq.3.23 is replaced by a central finite difference approximation:

$$\frac{\delta^2 T}{\delta x^2} = \frac{\delta}{\delta x}\left(\frac{\delta T}{\delta x}\right) \approx \frac{\frac{T_{i+1}^n - T_i^n}{\Delta x} - \frac{T_i^n - T_{i-1}^n}{\Delta x}}{\Delta x} = \frac{T_{i+1}^n - 2T_i^n + T_{i-1}^n}{(\Delta x)^2} \ . \tag{3.32}$$

Substituting equations 3.31 and 3.32 into Eq.3.23 and rearranging so all known quantities are on the right hand side of the equation(properties at n time step) we can compute the new temperature. Temperature at time n known form the thermocouple, therefore we can use Eq. 3.33 to compute the new temperature without solving any additional equations.

$$T_i^{n+1} = T_i^n + \alpha \Delta t \left(\frac{T_{i+1}^n - 2T_i^n + T_{i-1}^n}{(\Delta x)^2}\right) \ . \tag{3.33}$$

Eq. 3.33 can be rearranged defining $'r'$ stability factor:

$$T_i^{n+1} = T_i^n + \frac{\alpha \Delta t}{(\Delta x)^2}\left(T_{i+1}^n - 2T_i^n + T_{i-1}^n\right) \tag{3.34}$$

$$\mathbf{r} = \frac{\alpha \Delta t}{(\Delta x)^2} \tag{3.35}$$

$$T_i^{n+1} = \mathbf{r}T_{n+1}^n + (1 - 2\mathbf{r})\, T_i^n + \mathbf{r}T_{i-1}^n \ . \tag{3.36}$$

The FTCS scheme is easy to implement because the values of T_i^{n+1} can be updated independently of each other $n+1$ time point unknown. The entire solution is done in two loops: an outer loop for time steps, and an inner loop for the nodes of the grid at every time step. It is remarkable that, for the FTCS scheme, the value of T_i^{n+1} does not depend on T_{i-1}^{n+1} or T_{i+1}^{n+1} as they do in the BTCS and Crank-Nicolson schemes. Therefore, FTCS scheme behaves more like the solution to a hyperbolic differential equation than a parabolic differential equation.

The solutions to Eq.3.23 subject to the initial and boundary conditions are all bounded, decaying functions. In other words, the magnitude of the solution will decrease from the initial condition to a constant. The FTCS can yield unstable solutions that oscillate and grow if Δt is relatively big or Δx relatively small.

Stable solutions with the FTCS scheme are only obtained if [Morton and Mayers, 1994]:

$$\mathbf{r} = \frac{\alpha \Delta t}{(\Delta x)^2} \ . \tag{3.37}$$

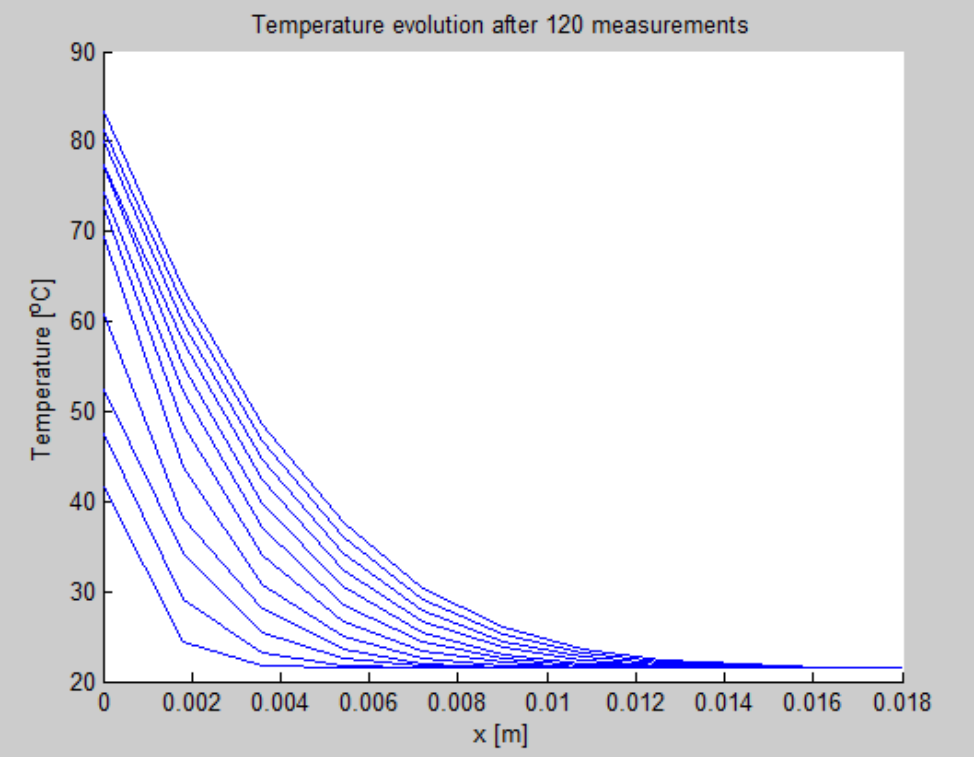

FIGURE 3.19: FDM of transient thermal profile.Taking $\alpha = 1.43x10^{-8}m^2/s$ [Quispe et al., 2011] and $nx = 10$ grid points, the stability factor is $\mathbf{r} = 0.4414 < \frac{1}{2}$ meeting the stability criteria.

Contrasting figures 3.19 and 3.12, the FDM predicts accurately how the temperature distributes within the phantom during the heating process. A plot showing the heating process in time is also explanatory (Fig. 3.20).

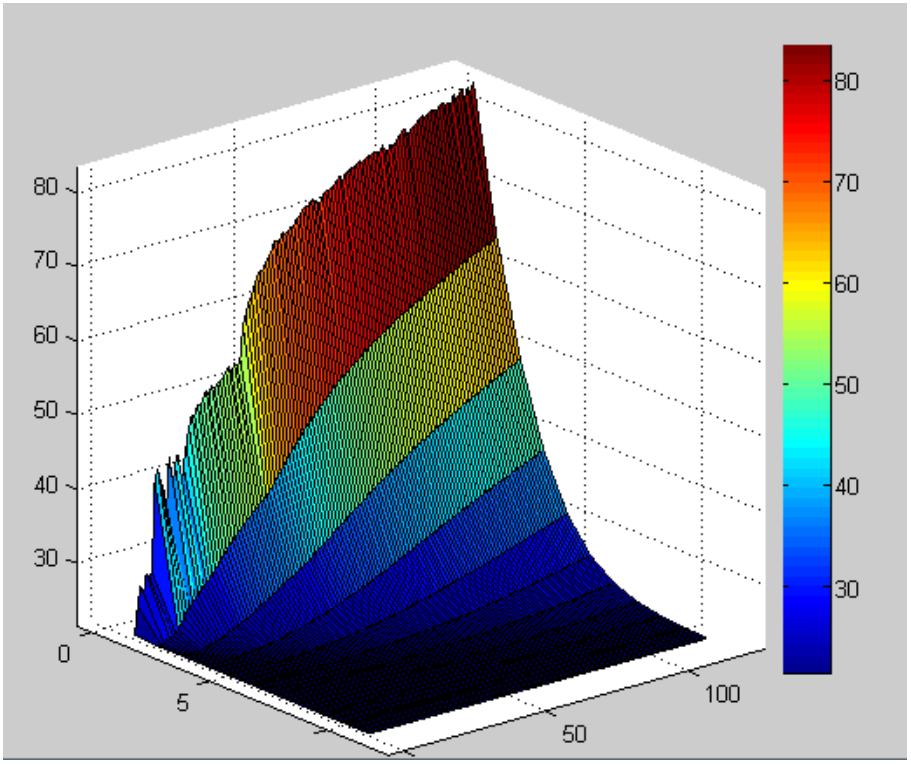

FIGURE 3.20: Plot of transient thermal profile in time.

3.1.5 Transient Heating Matlab PDE Solver

Using the PDE solver of Matlab we found also accuracy between the analytical solution, the FDM method and the experimental data.

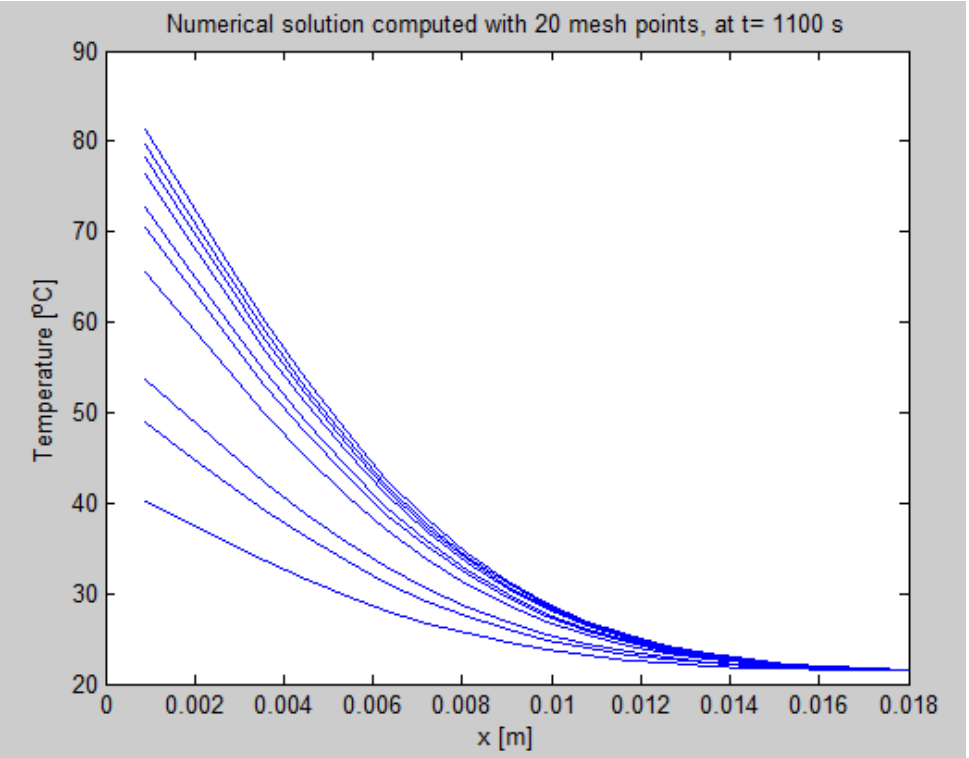

FIGURE 3.21: PDE solver thermal profile solution.

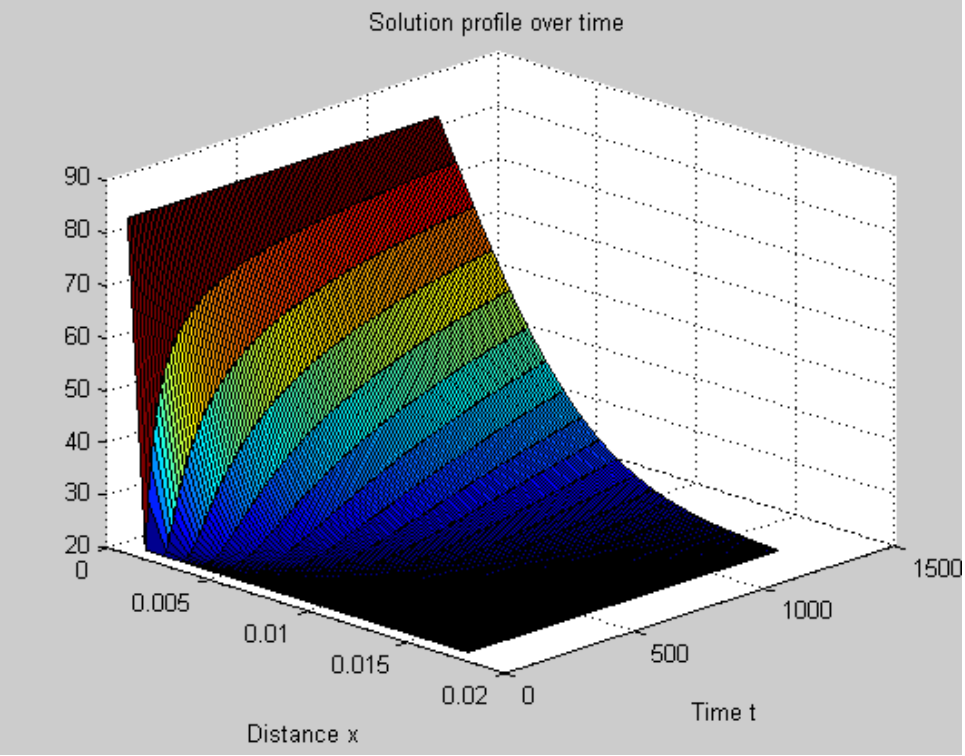

FIGURE 3.22: PDE solver thermal profile solution during the heating process.

This implementation has the advantage that is conditionally stable, in the graphs shown above the solution was refined with 20 grid points, instead of taking 10 grid points as in the previous finite difference method due to stability limitations.

3.2 Modeling Radio-frequency Ablation Heating

The problem of solving a radio-frequency (RF) heating process of agarose solutions phantoms is addressed in this section. Experimental data and results introduce the different modeling methods approached.

3.2.1 Experimental Radio-frequency Thermal Profile

Agarose solution phantoms were made to recreate the thermal and electrical conductivities of cardiac tissue in an ablation procedure. For this, a phantom with saline water and agar was built. Saline water is water and sodium chloride, which mimics electrical properties of real tissue in the phantom. The agar gel was made with 1.3-1.5 g of agar powder per every 100 ml of water. An electrode of 2.90 mm was used to induce electric current into the phantom. The tip of the electrode was cleaned with a file to ensure a proper coupling and a good electric current transmission to the phantom. Then, a thermocouple was coupled to the tip of the electrode (Fig. 3.23), by attaching the thermocouple to its side and fixing the thermocouple with adhesive tape so both tips concur at the same point (contact point).

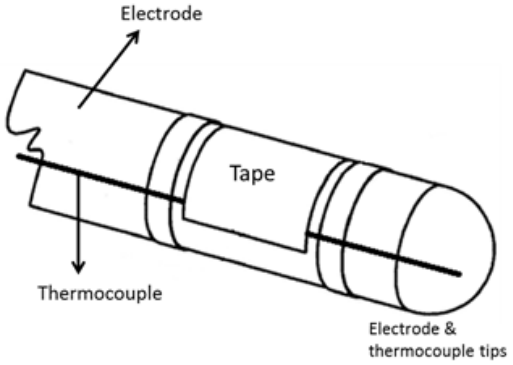

FIGURE 3.23: Diagram of the initial setup of the RF electrode.

The method to introduce the thermocouples in the phantom used in the experiment consisted on slicing the phantom evenly every 5mm. Each slide was checked for bumps or irregularities to be aware of the error that we could be working with the position of the thermocouples. Once cut, the thicker part was placed in the bottom of the water tank over foil paper that will come out of the recipient to make the electrical contact point, so the current flows through (Fig. 3.24). Then we placed a thermocouple in the center of the surface of the layer, and we covered it with the next phantom's layer. The latter process continues until we put the last and top layer that is in contact with the electrode and its thermocouple. All thermocouples were aligned in the vertical axis of the electrode.

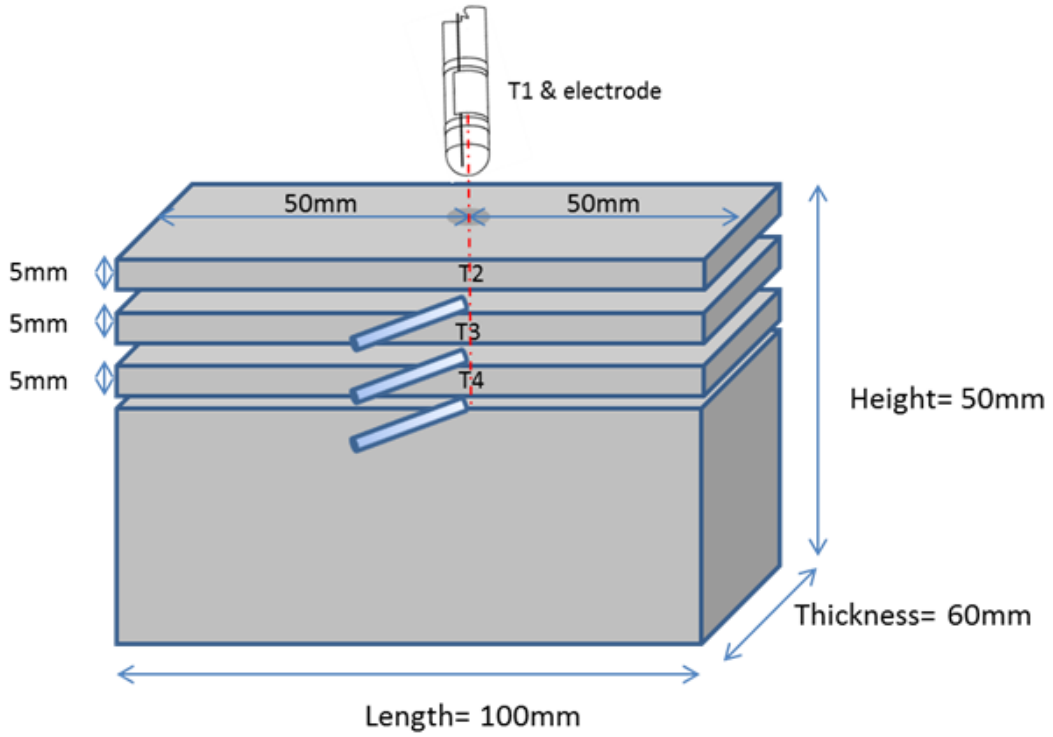

FIGURE 3.24: Diagram of the initial setup of the RF electrode.

For the electrical setup, see Fig. 3.25, we used a wave form generator providing a voltage peak to peak of $V_{pkpk} = 10$V with a frequency of $f = 10$kHz. The generated signal was amplified and induced into the phantom by the electrode. The phantom behaves as a resistance for the electric current and thus the temperature of the phantom is increased due to current flow. To measure the current flowing within the phantom we set the multimeter so the current went through it in a series circuit. The voltage drop was measured by a second multimeter electrically conected in parallel to the phantom.

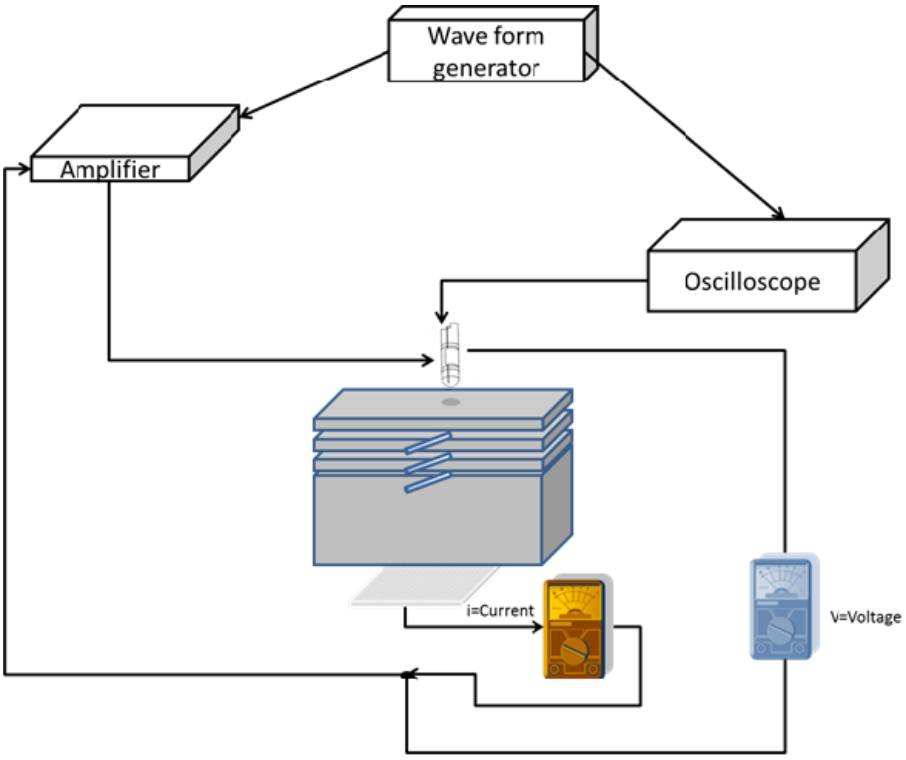

FIGURE 3.25: Diagram of the electrical setup for the RF heating process.

The temperature profile obtained in the RF heating process previously described is shown in Fig. 3.26. Measurements were made every $\Delta t = 10$s.

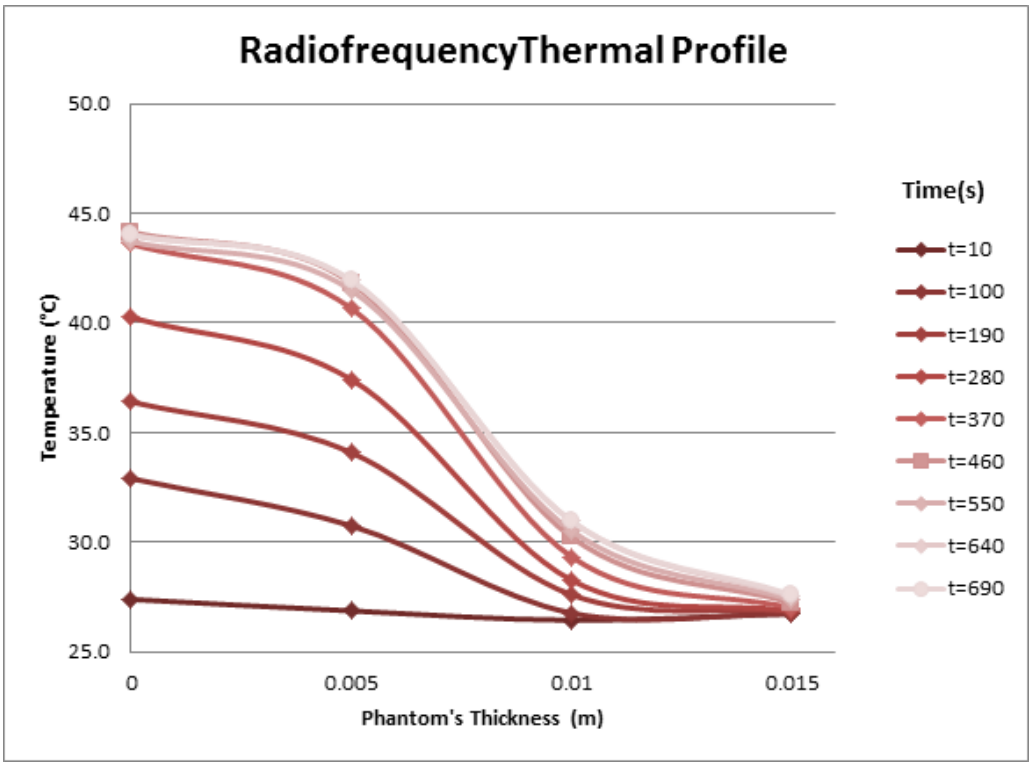

FIGURE 3.26: Radiofrequency heated phantom thermal profile, plot until deepest thermocouple depth (0.015 m).

By looking to Fig. 3.26 one can notice that the second half of the thermal profile could be approached by a transient heating process. On the other hand, the temperature distribution differs from the conductive heating process in a region close to the electrode. This most likely indicates that most of the electrical energy is deposited in the proximity of the electrode while the heating of the rest of the phantom is mainly to conductive heat transfer.

3.2.2 Radio-frequency Model Approaches

The change in temperature during ablation at any point in the tissue is given by the heat transfer equation called 'Modified Pennes Bioheat Equation' [Panescu et al., 1995]

$$\rho c \frac{\partial T}{\partial t} = \nabla \cdot k \nabla T + \mathbf{JE} - h_{bl}(T - T_{bl}) - Q_{el} \qquad \text{(2.1 revisited)}$$
$$h_{bl} = \rho_{bl} c_{bl} w_{bl} \ ,$$

where ρ is the mass density, c is the heat capacity, k is the thermal conductivity, $\mathbf{J}$ is the current density, $\mathbf{E}$ is the intensity of the electric field, ρ_{bl} is the blood density, c_{bl} is the blood heat capacity, w_{bl} is the blood perfusion, T_{bl} is the blood temperature, and Q_{el} accounts for the heat exchanged between the tissue and the ablation electrode. Q_{el} will be considered negligible. Our studies are made on agarose solution phantoms in a static water tank and thus blood perfusion factors will be considered negligible as well.

RFA probes operate between 350-550 kHz. At these frequencies, the wavelength of the electromagnetic energy is several orders of magnitude larger than the size of the ablation electrodes. Thus, the primary mode of energy transfer is through electrical conduction and can be modeled as a coupled quasi-static electrical conduction and heat conduction problem. The current density and the electric field intensity can be computed from the Laplace equation as [Chang and Nguyen, 2004]

$$\nabla \cdot \sigma(T) \nabla V = 0 \ , \qquad \text{(2.2 revisited)}$$

where ∇ is the gradient operator, $\sigma(T)$ is the temperature-dependent conductivity (Siemens/meter), and V is the electric potential (Volts).

The modifed Pennes Bioheat Equation can be seen as the conductive heating governing equation but also accounting for the electrical energy input (**JE**). Using the Matlab code for the conductive heating transfer case was the first strategy followed. However, the term **JE** will be different depending of which electric field distribution is considered within the phantom. Different FDM implementations using Matlab for RF heating were made considering different electric field distributions, such as spherical or spherical shelled. The FTCS scheme implemented in

Matlab was giving unstable solutions for the RF heating case. The FDM stability condition was meeting the conductive FDM stability criteria but it might have changed now that we were accounting for RF energy.

3.2.2.1 Spherical coordinates

Finite element method software (FEM) COMSOL is used to model the electric field distribution within the phantom. COMSOL results are presented in Fig. 3.27. We are going to work with symmetry in both poloidal and azimuthal angles for the electric field distribution.

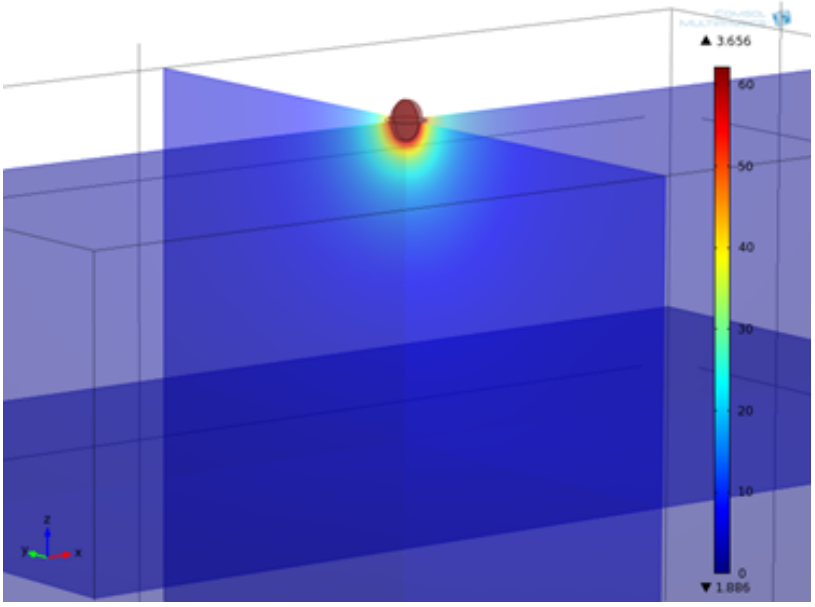

FIGURE 3.27: Electric field distribution of a spherical electrode.

Taking Pennes equation, assuming that blood perfusion and metabolic heat are negligible, follows

$$\rho c \frac{\delta T}{\delta t} = k\nabla^2 T + \mathbf{JE} \ , \tag{3.38}$$

where ∇^2 is the Laplacian operator. The Laplacian operator for Cartesian coordinates is

$$\rho c \frac{\delta T}{\delta t} = k\frac{\delta^2 T}{\delta x^2} + k\frac{\delta^2 T}{\delta y^2} + k\frac{\delta^2 T}{\delta z^2} + \mathbf{JE} \ . \tag{3.39}$$

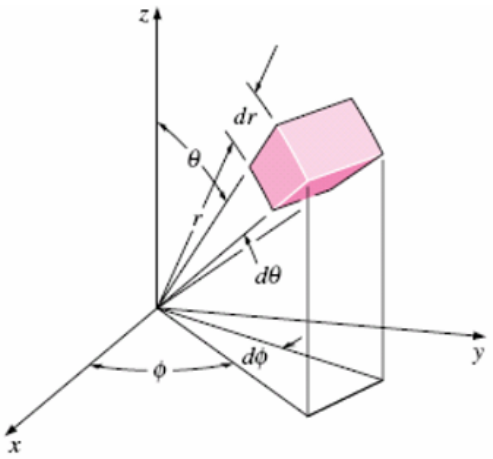

FIGURE 3.28: Reference system for spherical coordinates.

Considering the Laplacian operator for spherical coordinates (Fig. 3.28), we obtain the bio-heat equation for this coordinate systems

$$\rho c\frac{\delta T}{\delta t} = \frac{1}{r^2}\cdot\frac{\delta}{\delta r}\left(k\cdot r^2\frac{\delta T}{\delta r}\right)+\frac{1}{r^2 sin^2\theta}\cdot\frac{\delta}{\delta\varphi}\left(k\frac{\delta T}{\delta\varphi}\right)+\frac{1}{r^2 sin\theta}\cdot\frac{\delta}{\delta\theta}\left(k\cdot sin\theta\frac{\delta T}{\delta\theta}\right)+\mathbf{JE}\,, \tag{3.40}$$

where the temperature distribution of each point in space depends on its position and on the quantity of electrical energy input in that point. Having a Poloidal symmetry $\frac{\delta T}{\delta\theta}=0$ and an azimuthal symmetry $\frac{\delta T}{\delta\varphi}=0$ it follows

$$\rho c\frac{\delta T}{\delta t} = \frac{1}{r^2}\cdot\frac{\delta}{\delta r}\left(k\cdot r^2\frac{\delta T}{\delta r}\right)+\mathbf{JE}\,, \tag{3.41}$$

and rearranging

$$\frac{\delta T}{\delta t} = \frac{\alpha}{r}\left(2\frac{\delta T}{\delta r}+r\frac{\delta^2 T}{\delta r^2}\right)+\frac{\mathbf{JE}}{\rho c}\,. \tag{3.42}$$

Applying the FDM to $\frac{\delta T}{\delta t}$ and $\frac{\delta T}{\delta r}$

$$\frac{\delta T}{\delta t}=\frac{T_i^t-T_i^{t-\Delta t}}{\Delta t}\,;\frac{\delta T}{\delta r}=\frac{T_i^{t-\Delta t}-T_{i-1}^{t-\Delta t}}{\Delta r}\,;\frac{\delta^2 T}{\delta r^2}=\frac{T_{i+1}^{t-\Delta t}-2T_i^{t-\Delta t}+T_{i-1}^{t-\Delta t}}{(\Delta r)^2}\,, \tag{3.43}$$

where rearranging the temperature of the next time step can be calculated as

$$T_i^t = \frac{\Delta t \cdot \alpha}{r_i \cdot \Delta r} \cdot \left(\left(\frac{r_i}{\Delta r} \right) T_{i+1}^{t-\Delta t} + 2 \left(1 - \frac{r_i}{\Delta r} \right) T_i^{t-\Delta t} + \left(\frac{r_i}{\Delta r} - 2 \right) T_{i-1}^{t-\Delta t} \right) + \frac{\Delta t}{\rho c} \mathbf{JE} + T_i^{t-\Delta t} . \tag{3.44}$$

This solution is not stable for the FDM using the FTCS scheme. Changing the stencil of the FDM, i.e. using a Crank-Nicolson stencil instead of using a Forward in Time Centered in Space method, the solution has been shown to be more stable [Warming and Hyett, 1974]. One of the main factors that makes the Crank-Nicolson scheme more stable is that it uses more information, up to 6 points to calculate the next step against only 3 for the FTCS method implemented.

3.2.2.2 COMSOL Finite Element Method

The implementation of FEM using COMSOL software was made in order to have a model of the RF heating case. Same dimensions as for the voltage prediction shown in Fig. 3.27 were used. A temperature model was implemented and solved in COMSOL.

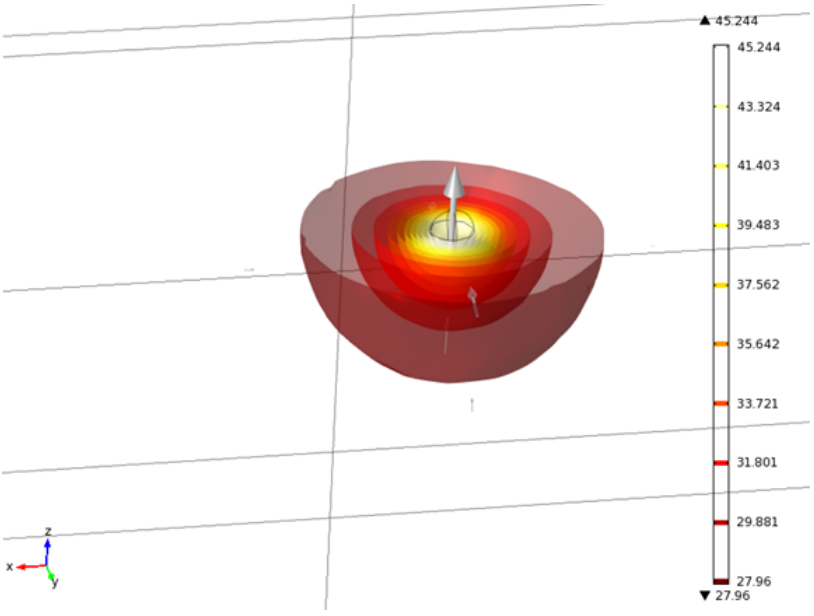

FIGURE 3.29: COMSOL temperature distribution. Results show axisymmetric symmetry.

The thermal profile distribution within the hypothetical location of the thermocouples is given by

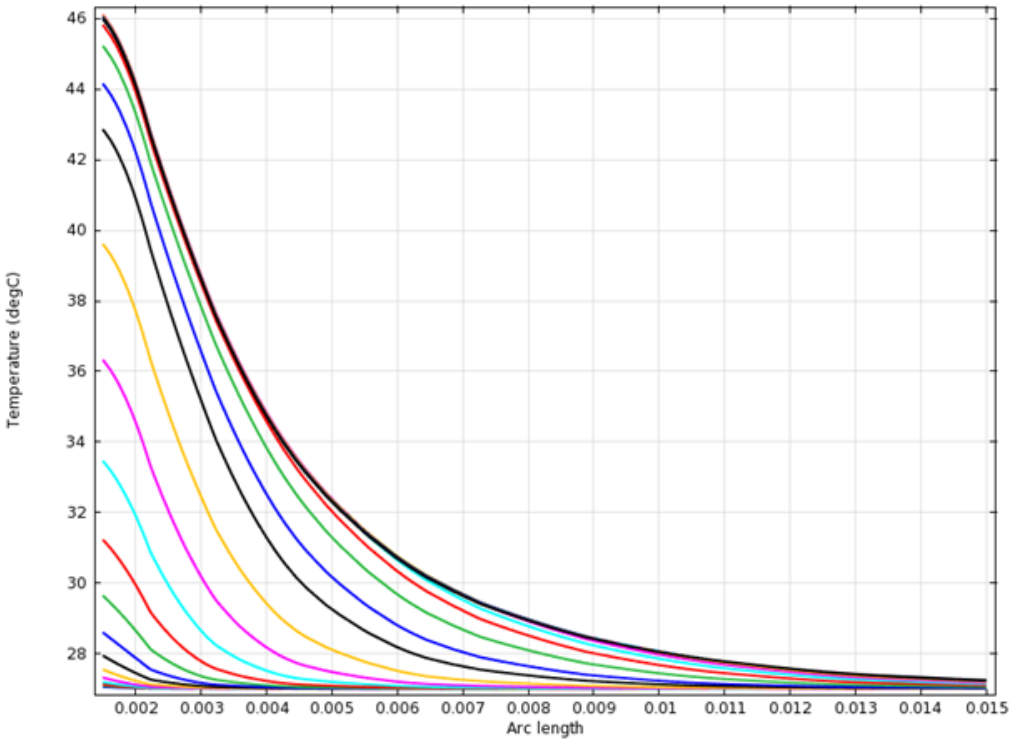

FIGURE 3.30: COMSOL Thermal Profile in the hypothetical location of the thermocouples.

COMSOL has a high computational cost but it reaches an accurate prediction of how a real process would behave. There are differences between COMSOL simulation and the experimental data (Fig. 3.26). Potential factors accounting for the difference between COMSOL model and our experimental data are the following

- Implementing a model in COMSOL has its own assumptions, such us the spherical shape of the electrode, the isotropic properties of the phantom, and also the accuracy of the physical properties used and those of the phantom.
- The RF energy input is a constant in COMSOL. While in the experiment the power was adjusted low at the first 100 s, and higher the last 500 s

controlling the temperature to be under 50°C in order not to have into account coagulation effects.

- The steady beginning in Fig. 3.26 in the RF experiment could be due to the insertion of the catheter inside the first agar layer without taking it into account.

Chapter 4

Optoacoustic Modeling

Non-invasive real-time measurement of temperature distribution in tissues during thermotherapy is necessary for the safe and efficient thermal destruction of tumors or other abnormal tissues.[Lehmann 1990, Welch and van Gemert 1995]. A wide variety of thermotherapy applications present associated to the lack of temperature control over the heated volume. Safe and efficient thermotherapy requires real-time temperature measurements with 1 mm spatial resolution and 1°C or better accuracy.

Infrared thermography is capable of real-time temperature measurements with an accuracy of 0.1°C. However, this technique can only measure the temperature at superficial tissue layers. On the other hand, ultrasound methods can provide real-time images with good resolution and depth of penetration, but they lack sufficient accuracy for temperature measurements [Seip and Ebbini, 1995]. Finally, MRI requires a long acquisition time to provide temperature mapping with high resolution and accuracy [Graham et al., 1998]. OA imaging has been developed and applied in many areas of biomedicine. It has been shown that time-resolved detection and analysis of the laser-induced pressure profiles allow for reconstruction of OA images and calculations of tissue temperature with an accuracy of about 17%. [Larina et al., 2005]

4.1 OA Pressure Temperature Dependence

The thermal expansion of an absorbing medium heated by a short laser pulse with an incident lase fluence F_0, induces a pressure rise P_0, in the irradiated volume upon stress confined irradiation conditions. [Gusev and Karabutov, 1993b]

$$P_0 = \left(\frac{\beta c_s^2}{C_p}\right)\mu_a F(z) = \Gamma\mu_a F(z) = \Gamma\mu_a F_0 e^{\left(-\mu_{eff}Z\right)} \ , \tag{4.1}$$

where β $[1°\mathrm{C}^{-1}]$ is the thermal expansion coefficient, c_s the speed of sound, C_p $\left[Jg^{-1}°\mathrm{C}^{-1}\right]$ the heat capacity at constant pressure, $F(z)$ $[Jcm^{-2}]$ the laser fluence and μ_a $[cm^{-1}]$ the absorption coefficient of the medium. The expression $\beta c_s^2/C_p$ represents the Grüneisen parameter, Γ(dimensionless). The factor $e^{\left(-\mu_{eff}Z\right)}$ represents exponential attenuation of the optical radiation in the medium. Therefore, the OA pressure is dependent on Γ, the fluence, and the optical properties of the medium. Equation 4.1 is valid under the condition of stress-confinement, when pressure relaxation is negligible during the heat deposition, achieved by using nanosecond optical pulses.

OA images are formed from the initial pressure rise $P(z)$ (Eq. 4.1). $P(z)$ is dependent on the grüneisen parameter Γ, the absorption coefficient μ_a and the fluence $F(z)$ which is dependent on μ_a itself. In this section, temperature effects on the different factors of the OA signal are studied.

4.2 Absorption Coefficient Temperature Dependence

Studying how the absorption coefficient μ_a is affected by temperature changes is relevant to know how much the OA signal P_0 changes due to temperature variations. In an ablation procedure, light is absorbed mainly by blood. In order to study the optical properties dependence on temperature we used a spectrometer.

The spectrometer measures optical density (OD), where for a non-scattering sample $\mu_a = 2.3 \cdot OD$. Light can be either absorbed, scattered or can go through the substance. Therefore, changes in OD detected by the spectrometer can be due to variations in the absorption coefficient μ_a or the scattering coefficient μ_s of the substance measured. The latter variations could take place at the same time and change the OD in the same direction or not.

In order to study the potential temperature variations of the absorption coefficient, several substances were used. Black India ink was used in the first place as an example of non-scattering medium. For a more practical applicability of the study, we also used haemoglobin and bovine blood.

4.2.0.3 Ink

An ink solution was first measured in the spectrometer because it has no scattering. Therefore changes in OD are proportional to changes in μ_a. We used an ink solution with an optical density of 1 OD, which was heated in a hot water bath. Several readings of the spectrometer were taken during the process of cooling down.

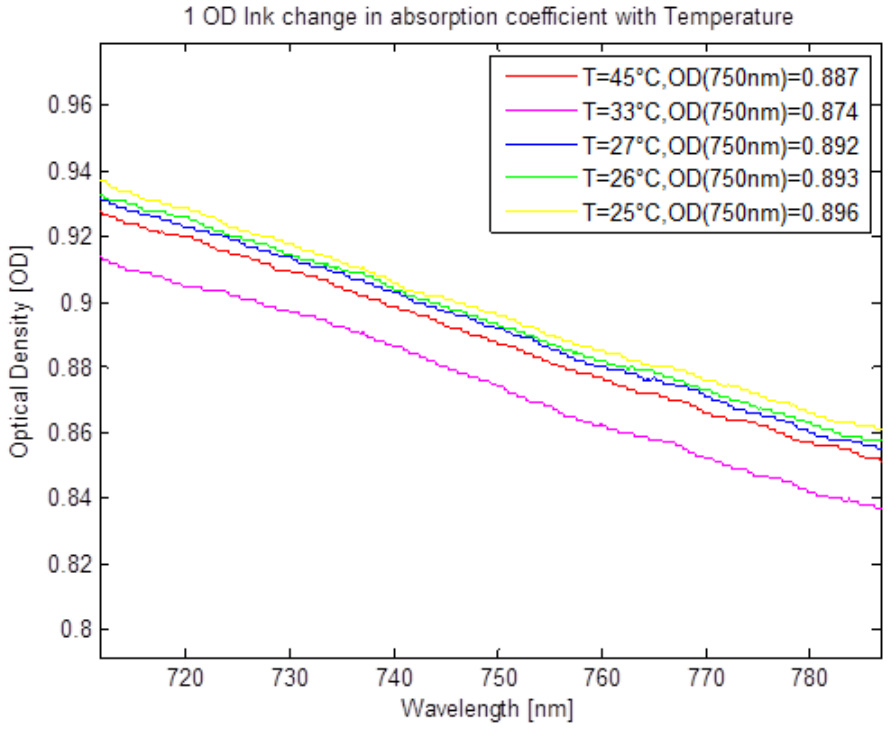

FIGURE 4.1: μ_a temperature dependence of 1 OD ink. 2% maximum variation.

The absorption coefficient of ink is shown for the temperature ($25 - 50°C$) and wavelength (750nm) ranges of interest (Fig. 4.1). The experimental data show a maximum variation of 2% in OD with an increase of 20°C, which is significant considering potential errors in the measurement.

4.2.0.4 Haemoglobin

As a substance similar to blood with no scattering effects, we used the absorption molecule of blood haemoglobin. Deoxyhaemoglobin (Hb) has no scattering. However, since oxygen gets instantly bounded to haemoglobin with its contact with air, it becomes oxygenated. Blood also contains other substances whose potential effects on optical properties are avoided by using oxyhaemoglobin (HbO_2).

The normal concentrations of haemoglobin in blood for adult males is 14 to 18g/dL or 0.14 to 0.18g/mL [Perkins and Hussong, 2001]. The solution with normal concentrations had presence of lumps that could affect the absorption of haemoglobin.

We studied the temperature dependence of the absorption coefficient using 25% of the normal concentration for adult males.

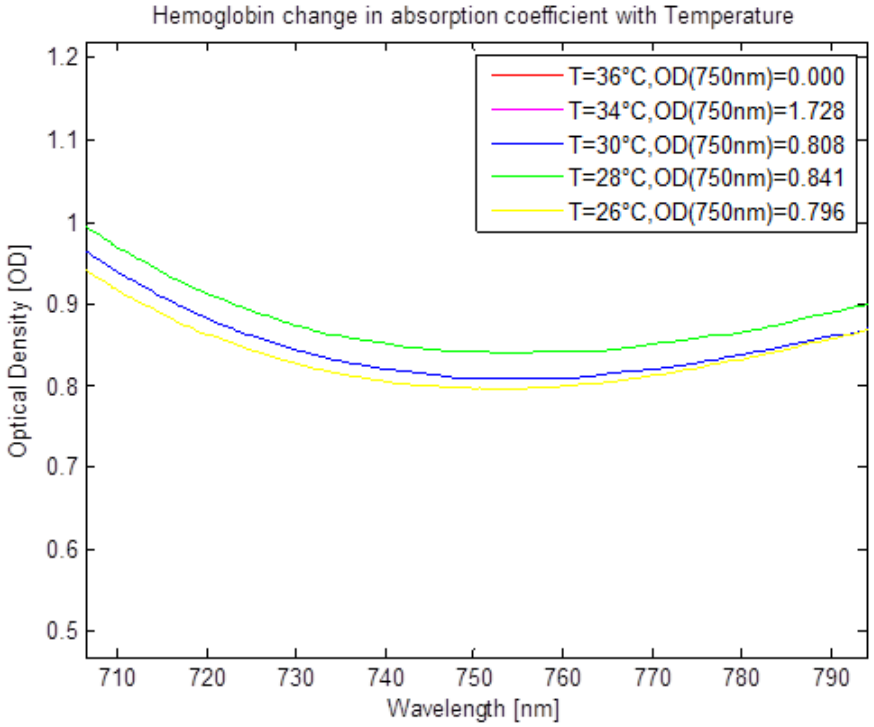

FIGURE 4.2: μ_a temperature dependence of Hb. 2% maximum variation.

OD readings of haemoglobin for $T = 34°C$ and $T = 36°C$ are not shown in the graph because those underwent coagulation when reaching temperatures above 50°C in the water bath.(Fig. 4.2)

4.2.0.5 Bovine Blood

Real blood has also optical scattering that can affect the OD measurement. The temperature variations in the scattering could be affecting the OD measurement in the same direction as the temperature changes of the absorption coefficient or in the opposite direction (balancing the change).

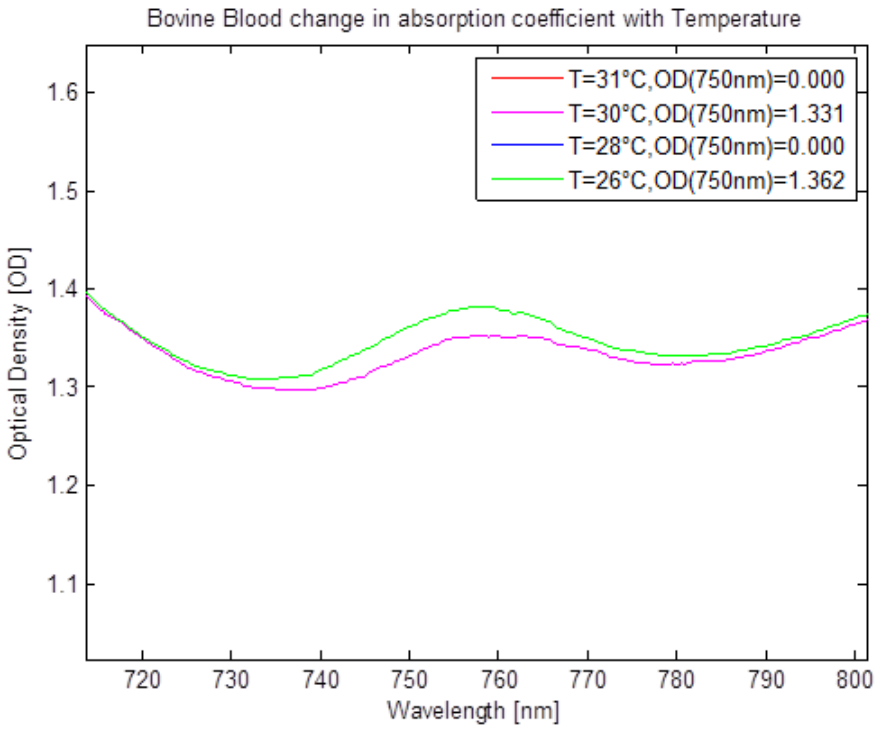

FIGURE 4.3: μ_a temperature dependence of bobine blood. 2% maximum variation.

In the same way as in the haemoglobin case, OD readings for $T = 28°C$ and $T = 31°C$ are not shown in the graph because those proves underwent coagulation reaching temperatures above 50°C in the water bath. However, $T = 31°C$ is shown, they were different proves. Coagulated probes were removed.(Fig. 4.3)

An increase from 26 to 30°C doesn't change significantly the OD of Blood. As blood has scattering, this can change the OD measurement. The absorption coefficient of blood could change in one direction the OD signal while the scattering would act in the opposite direction balancing and making invisible the variation in the absorption coefficient with temperature. However, from the results for substances that lack scattering as ink and haemoglobin, we can conclude that the absorption coefficient doesn't change significantly with temperature.

The conclusion of this experiment will reduce modeling complexity. If the absorption coefficient μ_a doesn't change with temperature, the dominant factor of the

OA signal changes with temperature is the Grüneisen parameter Γ.

4.3 OA signal change with temperature

We have shown in the previous section that the absorption coefficient doesn't increase significantly with temperature. The OA signal response to temperature is studied in this section.

We performed experiments in a commercial multispectral optoacoustic tomography (MSOT). MSOT is a new imaging modality that utilizes generation of ultrasonic waves by exciting the sample at multiple wavelength with ultrashort pulses of light in the imaged targets. [Razansky, 2012]. In our case, the laser wavelength was set to 750 nm. The MSOT scanner contains a water tank that needs to be filled to guarantee acoustic coupling between the sample and the ultrasound transducer.

The experiment was made with a cylindrical phantom with a polyethylene tubing embedded along its axis. We poured hot ≈1.2 OD ink through the tubing while OA images where being acquired. The phantom was made of agar and de-ionized water. The ink solution was heated in a water bath and poured through the phantom using a syringe. The temperature of the water was 34°C while the hot ink solution was about 40°C.

Before inserting the ink solution, as there were no absorbing molecules in the phantom, the OA image contains only noise (Fig. 4.4).

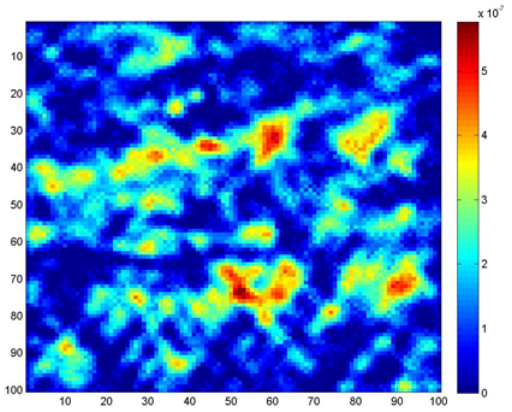

FIGURE 4.4: MSOT frame showing no specific absorption zone.

When the ink was being injected, the OA image started to focus in the tubing position.

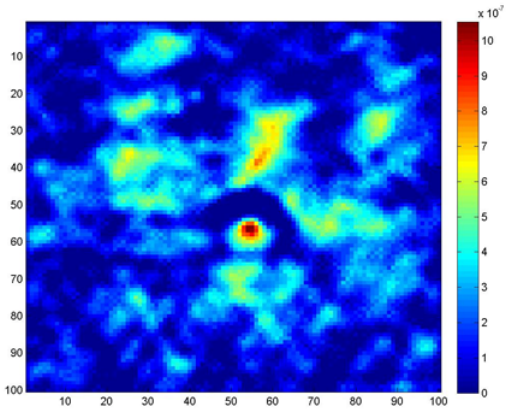

FIGURE 4.5: MSOT ink injection frame time, OA signal gets absorbed by ink.

Once the ink was flowing through the tube it stabilized the OA signal. OA signal changes in the tubing are due to temperature differentials.

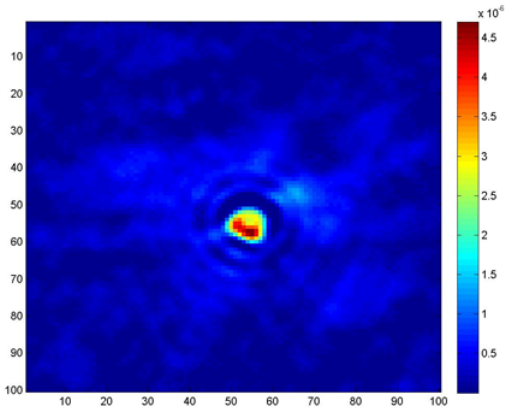

FIGURE 4.6: MSOT OA signal once ink is running through the phantom.

The figures depicted above are 3 frames that describe 3 phases of the injection of the ink. Studying all the frames and taking the pixel with the maximum value of the signal for every frame and plotting the value of this pixel, we get the maximum value of the OA signal in time.

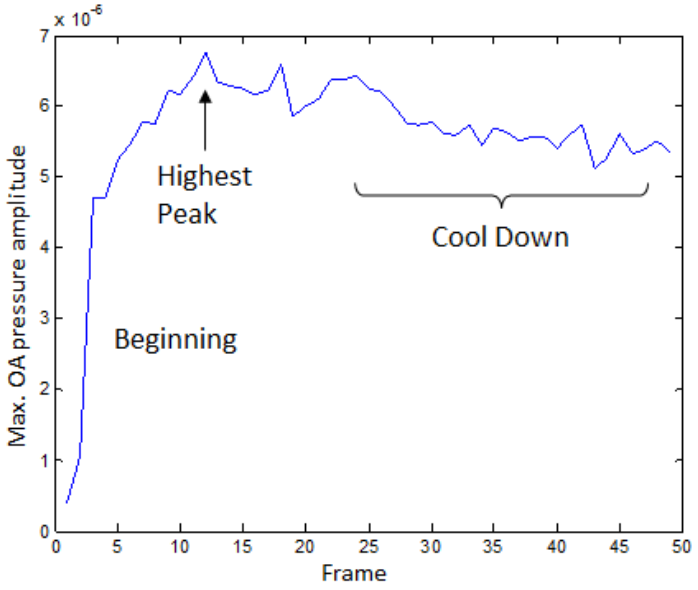

FIGURE 4.7: Maximum value of MSOT OA signal in time.

The OA response to temperature is observed in Fig. 4.7. The OA signal is around zero before injection(Fig. 4.4). When ink is injected the OA signal spiked until

a value that is lower than the maximum of the graph in Fig.4.7. The ink was poured in the tubing with a syringe previously heated in a hot water bath.The lower OA amplitude at the beginning of the acquisition sequence corresponds to the tip of the syringe, which cools down toroom temperature before the rest of the syringe while inserting it in the tubing. Then the OA signal rises until the highest peak. Then the phantom starts to absorb more heat from the tubing and the temperature inside such tubing decreases. Form the shift in the OA signal we can observe that at least it changes 14.3% in amplitude with only 6°C temperature increment. On the other hand, the absorption coefficient shift with temperature was less than 2% for a 20°C temperature increment.

We can conclude that OA signal significantly increases with temperature while the absorption coefficient does not change significantly even with a considerable increase in temperature. The Grüneisen parameter is the dominant factor in the OA signal changes with temperature.

IAn additional experiment was performed to corroborate these findings in a more controlled manner. For this, we studied how the OA signal measured with a single element transducer changes with temperature. The experimental setup consistedof a 15 MHz transducer and a tubing located at a distance of approximately 35mm. Both the transducer and the tubing were inmersed in a water tank. The laser wavelength was set to a 720nm laser and a pulse repetition frequency of 100 Hz was used. Each signal was averaged 1000 times. Black India ink was poured through the tubing while modifying the temperature of the water bath with ice.

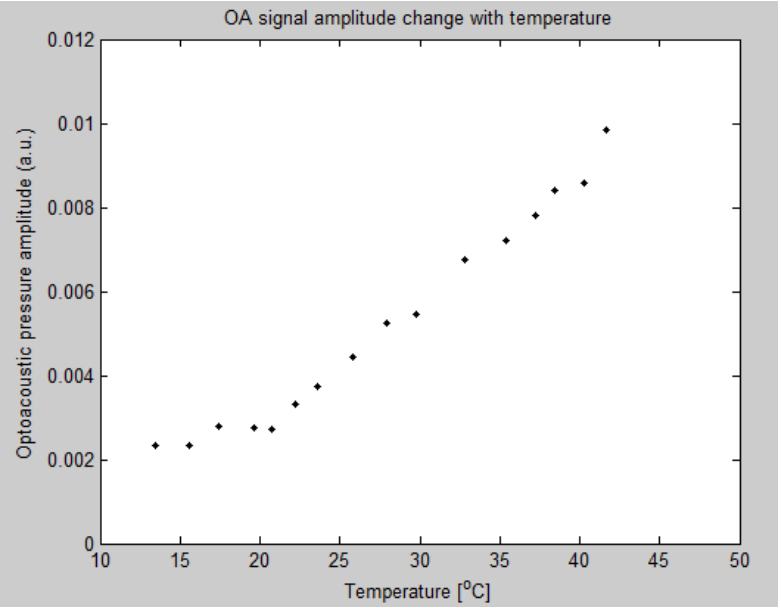

FIGURE 4.8: OA pressure amplitude with temperature.

The measured OA signal amplitude as a function of temperature is shown in Fig.4.8. The change in the OA signal is approximately linear with temperature (Fig. **??**) as the Grüneisen does. Furthermore, experiments have shown a very strong OA signal increase with an $\Delta T = 10°\text{C}$ while the absorption coefficient μ_a changed less than 2% with an $\Delta T = 20°\text{C}$. We can then conclude that the Grüneisen parameter is the dominant factor governing OA signal changes with temperature.

Chapter 5

Conclusions and Future Research

5.1 Conclusions

The main purpose of this thesis was to demonstrate capabilities of OA imaging in temperature monitoring during RF ablation, giving feedback so that temperature maps of the tissue can be obtained during future ablation experiments. The results obtained show that indeed OA signals are strongly affected by temperature due to the temperature dependence of the Grüneisen parameter. Thereby, an efficient design of an optoacoustic imaging system to be incorporated in RF ablation interventions as well as the development of accurate thermal models to estimate the temperature distribution from the optoacoustic readings can allow significantly improving the outcome of these medical procedures.

Accurate thermal models based on transient heat transfer theory were developed analytically. Numerical methods based on finite difference and finite element methods were also analyzed. It was shown that numerical methods can be used for accurate modeling of the experimental distribution of temperature as they match the analytical solutions forspecific cases. Experimental results further validated the thermal models employed.

On the other hand, it was shown that the OA signals increase with temperature is not significantly influenced by the absorption coefficient. Indeed, the Grüneisen

parameter is the dominant factor in the temperature dependence of the OA signals. Then, the OA signals provide a means to monitor temperature through variation in the Grüneisen parameter.

Overall, we expect that the results shown in this work have impact in the investigation of RF ablation monitoring procedures, which represent an unsolved problem in different types of medical interventions, particularly in the treatment of arrhythmias of the heart.

5.2 Future Research

Future research is required to develop a temperature-dependent OA model which considers the effects of temperature on Grüneisen parameter. The coupled model can be used to calibrate optoacoustic images and reconstruction algorithms to achieve accurate optoacoustic images for controlled temperature changes less than 50 °C,so the change in absorption coefficient due to tissue damage does not have to be considered.

More accurate modeling for RF heating implies considering other parameters substantially dependent on temperature, e.g. conductivity $\sigma(T)$. Further experimental validation with more advance optoacoustic monitoring system is also a future step of the work presented in this thesis.

Bibliography

Y. H. Kim, G. Sosa-Suarez, T. G. Trouton, S. S. O'Nunain, S. Osswald, B. A. McGovern, J. N. Ruskin, and H. Garan. Treatment of ventricular tachycardia by transcatheter radiofrequency ablation in patients with ischemic heart disease. *American Heart Association*, 1994. doi: 10.1161/01.CIR.89.3.1094.

L. V. Wang and H. Wu. Biomedical optics, principles and imaging. 2007.

P. C. Beard. Biomedical photoacoustic imaging. *Interface Focus*, 72(1):602–631, June 2011. doi: 10.1098/rsfs.2011.0028.

William J. Mandel. Cardiac arrhythmias: Their mechanisms, diagnosis, and management (3 ed.). *Lippincott Williams and Wilkins*, 62, 1995.

D. Panescu, J. G. Whayne, S. D. Fleischman, M. S. Mirotznik, D. K. Swanson, and J. G. Webster. Three-dimensional finite element analysis of current density and temperature distributions during radio-frequency ablation. *Transcations on Biomedical Engineering*, (9):879–890, 1995. doi: 0018-9294/95$04.00.

I. A. Chang and U. D. Nguyen. Thermal modeling of lesion growth with radiofrequency ablation devices. *Biomedical Engineering Online*, 2004. doi: 10.1186/1475-925X-3-27.

B. T. Cox and P. C. Beard. Fast calculation of pulsed photoacoustic fields in fluids using k-space methods. *Department of Medical Physiscs and Bioengineering, UNiversity College of London, Gower Street*, 2004.

B. T. Cox and C. P. Beard. Fast calculation of pulsed photoacoustic fields using k-space methods. *Acoust. Soc. Am.*, (117):3616–3636, 2005. doi: 10.1121/1.1920227.

C. L. Tsai, J. C. Chen, and W.J. Wang. Near-infrared absorption property of biological soft tissue constituents. *J. Med. Biol. Eng.*, 21(1):7–14, 2001.

R. A. Kruger, R. B. Lam, D. R. Reinecke, S. P. Del Rio, and R. P. Doyle. Photoacoustic angiography of the breast. *Med. Phys*, 6096(37), 2010. doi: 10.1118/1.3497677.

G. Ku and L. V. Wang. Deeply penetrating photoacoustic tomography in biological tissues enhanced with an optical contrast agent. *Opt. Lett*, (30):507–509, 2005. doi: 10.1364/OL.30.000507.

K. Homan, S. Kim, Y. S. Chen, B. Wang, S. Mallidi, and S. Emelianov. Prospects of molecular photoacoustic imaging at 1064 nm wavelength. *Opt. Lett.*, (35): 2663–2665, 2010. doi: 10.1364/OL.35.002663.

V. E. Gusev and A. Karabutov. Laser optoacoustics. *New York: AIP*, 1993a.

I. V. Larina, K. V. Larin, and R. O. Esenaliev. Real-time optoacoustic monitoring of temperature in tissues. *Journal of physics D: Applied Physics*, 2005. doi: 10.1088/0022-3727/38/15/015.

J. R. Welty, C. E. Wicks, R. E. Wilson, and G. L. Rorrer. *Fundamentals of Momentum, Heat and Mass Transfer 5th Edition.* 2007.

Y. A.Çengel. *HEAT AND MASS TRANSFER: A PRACTICAL APPROACH.* 2006.

K. W. Morton and D. F. Mayers. Numerical solution of partial differential equations: An introduction. *Cambridge University Press*, 1994.

L. V. Quispe, A. C. Loeza, J. A. Gil, and P. Q. Owen. Diffusion of methylene blue in phantoms of agar using optical absorption techniques. *In Tech*, 2011.

R. F. Warming and B. J. Hyett. The modified equation approach to the stability and accuracy analysis of finite-difference methods. *Journal of Computational Physics*, pages 159–179, 1974. doi: 10.1016/0021-9991(74)90011-4.

R. Seip and E. S. Ebbini. Noninvasive estimation of tissue temperature response to heating fields using diagnostic ultrasound. *IEEE Trans. Biomed. Eng.*, (42): 828–839, 1995.

S. J. Graham, M. J. Bronskill, and R. M. Henkelman. Noninvasive estimation of tissue temperature response to heating fields using diagnostic ultrasound. *Magn. Reson. Med.*, (39):198–203, 1998.

V. E. Gusev and A. Karabutov. Laser optoacoustics. *AIP*, 1993b.

S. L. Perkins and J. W. Hussong. Red blood cells. *In: Jones SL, ed. Clinical Laboratory Pearls, Philadelphia, PA*, pages 61–96, 2001.

D. Razansky. Multi-spectral optoacoustic tomography – volumetric color hearing in real time. *IEEE J. Sel. Topics Quantum Electron*, pages 1234–1243, 2012.